Journal of Materials Research and Technology 37 (2025) 671–686

Contents lists available at ScienceDirect

Journal of Materials Research and Technology

journal homepage: www.elsevier.com/locate/jmrt

A combined experimental and numerical assessment of the role of microsegregation and phase formation on hot cracking susceptibility in laser powder bed fusion processed CM247LC

Philipp Stich[a], Markus Apel[b], Mustafa Megahed[c], Ludo Bautmans[d], Pere Barriobero Vila[e], Marcus Hans[f], Thomas Weirich E.[g], Klaus Büßenschütt[h,*], Johannes Henrich Schleifenbaum[h], Christian Haase[i]

[a] *EOS - Electro Optical Systems, Robert-Stirling-Ring 1, 82152, Krailling, Germany*
[b] *Access e.V., Intzestr. 5, 52072, Aachen, Germany*
[c] *Consultant, Germany*
[d] *Oerlikon Surface Solutions AG, Pfäffikon, Branch Balzers, 9496, Balzers, Liechtenstein*
[e] *Department of Materials Science and Engineering, Technical University of Catalonia, Carrer de Jordi Girona 31, 08034, Barcelona, Spain*
[f] *Materials Chemistry, RWTH Aachen University, Kopernikusstraße 10, 52074, Aachen, Germany*
[g] *Central Facility for Electron Microscopy, RWTH Aachen University, Ahornstr. 55, 52074, Aachen, Germany*
[h] *Digital Additive Production, RWTH Aachen University, Campus-Boulevard 73, 52074, Aachen, Germany*
[i] *Chair Materials for Additive Manufacturing, TU Berlin, Ernst-Reuter-Platz 1, 10623, Berlin, Germany*

ARTICLE INFO

Handling Editor: L Murr

Keywords:
Additive manufacturing
Phase-field method
Nickel
Superalloy
Micro segregation
Hot cracking

ABSTRACT

For many high-performance alloys originally developed for the casting route, hot cracking is a serious problem in the Laser Powder Bed Fusion (PBF-LB/M) process and limits the use of e.g. high-γ' nickel-based alloys such as CM247LC in additive manufacturing. In this work, we investigate the relationship between PBF-LB/M processing parameters and the solidification path, i.e. phase formation and microsegregation, and its potential impact on hot cracking for the high-γ' alloy CM247LC. We combined experimental microstructural analysis using scanning and transmission electron microscopy, atom probe tomography and diffraction techniques with multiphase-field simulations on μm scale. Process simulations at mesoscale of the melt pool provide the link between the process conditions and the thermal boundary conditions for the microstructural simulations. The study confirms the appearance of carbides, borides and γ'-precipitates in the as-solidified microstructure. The quantity and particle size of these phases as observed in the experimental samples, are in qualitative agreement with the simulation results. Therefore, the simulations can be used to elucidate and quantify the differences in the solidification path for different thermal process conditions. Although the comparison of samples processed with high energy density (cooling rate 65,000 K/s) with those processed with low energy density (cooling rate: 570,000 K/s) show large differences in the crack density observed in the experiments, the microstructural differences and the phase formation at the dendritic scale do not show any remarkable qualitative or quantitative differences. The correlation between processing conditions, microstructure evolution and crack formation is critically discussed and differences to the current understanding presented in existing literature are identified.

1. Introduction

Additive Manufacturing (AM) technologies offer greatly enhanced design flexibility compared to conventional manufacturing processes, due to the incremental, layer-by-layer manufacturing approach. This enables the production of near-net-shape components with complex geometries, such as inner cooling channels, enabling higher operating temperatures for turbine blades. Furthermore, the layer-by-layer process opens up the possibility to control local mechanical properties by local process parameter variations, if the process-microstructure-property relationship is well understood [1–7].

Nickel-based superalloys provide excellent creep and fatigue

---

* Corresponding author.
E-mail address: klaus.buessenschuett@dap.rwth-aachen.de (K. Büßenschütt).

https://doi.org/10.1016/j.jmrt.2025.06.040
Received 22 April 2025; Received in revised form 5 June 2025; Accepted 5 June 2025

strength at elevated temperatures, while exhibiting good oxidation and corrosion resistance [8–10]. These alloys are typically highly alloyed to maximize strengthening through carbide formation, solid solution strengthening and a high volume fraction of γ'-$Ni_3(Al,Ti)$ precipitates. Originally, most nickel-based superalloys were tailored for low cooling rate casting processes. At high cooling rates and cyclic remelting in PBF-LB/M, in particular alloys with a high γ' fraction are prone to cracking. This makes their integration into AM processes a major challenge. The PBF-LB/M process is characterized by high cooling rates and large thermal gradients, which lead to high internal stresses during the build process and cause detrimental defects such as cracking and delamination. Common ways to reduce the cracking susceptibility are e. g. preheating, to search for optimized process conditions, such as energy input or scanning strategies, or by modifying the alloy itself, i.e. changing its chemical composition [11–17].

Up to now, the precise correlation between process parameters and crack formation remains an open question, as different cracking mechanisms overlap, and some of the underlying mechanisms are yet to be fully understood. Potential cracking mechanisms, as discussed in literature, are solidification cracking (SC), liquation cracking (LC), ductility dip cracking (DDC), and strain-age cracking (SAC). SC and LC are categorized as hot cracks, given that cracking takes place in the presence of a liquid phase. Often SC is correlated with alloys showing a large solidification interval. The crack formation takes place in the last stages of the solidification process when the mushy zone morphology reaches a point of forming an interconnected solid skeleton. In this stage, the decreasing permeability in the mushy zone can lead to isolated liquid regions, where the interdendritic filling of the remaining liquid does not compensate volume changes due to solidification shrinkage or the response to any other thermomechanical stress acting on the mushy zone [18]. A liquid film cannot withstand the high stresses and cracks form. The LC mechanism involves local variations of the solidus temperature caused by microsegregation of alloying elements. This may lead to local melting within the heat-affected-zones (HAZ) of subsequent hatches or layers. The other two mechanisms are linked to solid-state phenomena. DDC results from material rupture due to a low ductility within a specific temperature range. SAC predominantly occurs during heat-treatment, driven by resultant stresses originating from precipitation [19].

Process parameters strongly influence the thermal history of the PBF-LB/M manufacturing process. Numerous studies focus on the optimization of PBF-LB/M process parameters to minimize in-process crack formation [12,13,20–24]. Carter et al. [25] investigated the correlation of the volumetric energy density $\left(\frac{J}{mm^3}\right)$ and the resulting crack density across several studies for PBF-LB/M-processed CM247LC. No clear trend was found in the data and the interaction between laser power, scanning speed and hatch spacing remained unclear. In another study, Carter et al. [19] found a decrease in crack density of CM247LC samples, when the scanning speed of the laser beam was increased. The influence of the hatch distance was less clear. Depending on the other process parameters, increasing the hatch distance resulted in more or less cracks. In a more recent study, Carter et al. [15] showed that the island exposure strategy has a detrimental effect on crack density. It is stated that the overlap regions of the exposure result in an isotropic microstructure with numerous high-angle grain boundaries (HAGB). Other studies also highlight the effect of HAGBs on cracking for Ni-based superalloys [26, 27]. Hariharan et al. [28] showed that in PBF-LB/M IN738LC, cracks occur exclusively at HAGBs. No cracks were found at low-angle grain boundaries. The authors reasoned that this is due to the increased accumulation of zirconium, carbon, boron and silicon, and, thus, a higher grain boundary energy (γ_{GB}) and solid-liquid interfacial energy (γ_{SL}) at HAGBs. In a first study, Fardan et al. [20] linked the process parameters to the defect structure of CM247LC. The results showed the dependence of cracks not from single processing parameters, but from the linear energy density (laser power/process speed). A small linear energy of 0.1 results in shallow and narrow melt pools, smaller grains and consequently the lowest crack density. The resulting crack density is with 0.74 mm/mm^2 still too high for application in high-performance components and only a few parameter sets were investigated. Wang et al. [29] established a thermal model and showed that the calculated maximum melt pool temperature correlated with the corresponding crack density. In comparison, the crack density only correlated poorly with different energy input metrics, highlighting the importance of additional information acquired through computational efforts.

Although a first conclusion on the impact of processing parameters on the defect structure of CM247LC was drawn, only a few parameter combinations within a small processing window were investigated and no processing window for crack-free PBF-LB/M of CM247LC has yet been identified. A comprehensive experimental and simulative analysis is still missing in literature. In addition, a complete understanding of the correlation between process parameters and the resulting microstructure in terms of formation and formation sequence of phases at the end of solidification is lacking.

The experimental basis in this study is a PBF-LB/M process parameter study for CM247LC. A systematic parameter variation with varying laser power, scanning speed and hatch distance is correlated with the resulting defect fractions and distributions. The parameters are based on industrial applicability and, therefore, no pre-heating is applied. Semi analytic and computational-fluid-dynamics-based (CFD) process simulations are used to calculate spatially resolved thermal process conditions such as cooling rate, temperature gradient and melt pool dimensions. The temperature evolution from the process simulation is then used as thermal boundary conditions for microstructure simulation using the multiphase-field method. The emerging phases and the microsegregation pattern as predicted by the phase-field simulations are semi-quantitatively compared to analytic data acquired by scanning transmission electron microscopy (SEM) combined with transmission electron microscopy - energy dispersive X-ray spectroscopy (TEM-EDS), atom probe tomography (APT) and high-energy synchrotron X-ray diffraction (HE-XRD) measurements.

2. Applied methods

2.1. Material and sample preparation

The composition of the superalloy CM247LC used in this study is given in Table 1. The composition of the as-received powder was measured using inductively coupled plasma-optical emission spectroscopy (ICP-EOS). The C content was determined via combustion analysis. The morphology of the powder reveals mainly spherical shaped particles. No hollow powder particles or significant satellites were detected. The particle size distribution ranges between D_{10} 19.9 and D_{90} 42.3 μm with a median particle size D_{50} of 31.1 μm.

Cubic specimens with a size of 10 × 10 × 10 mm^3 were printed on an EOS (EOS GmbH, Munich) M290 system equipped with a Yb:YAG-laser (maximum output power of 400 W) in argon atmosphere. Minitab20 software (Minitab GmbH, Munich) was used to define three full-factorial design experiments, resulting in over 200 combinations of the process parameters: laser power, scanning speed and hatch distance. The energy density input ranges from 27.06 to 226.19 J/mm^3. Table 2 gives an overview of the process parameters as well as the parameter ranges for the three different states: high power (HP), high speed (HS) and low power (LP). Soft recoating, a stripe width of 10 mm and the standard spot size of 80 μm were used. Each subsequent layer is rotated by 67°. A layer thickness of 30 μm was kept constant.

2.2. Microstructure characterization

The PBF-LB/M cubic samples were cut in half in building direction and embedded for further microstructural analysis. Afterwards, the samples were grinded and finally polished with 1 μm diamond

Table 1
The composition of the superalloy CM247LC investigated in this study in wt.% and at.%. The material was provided by Höganäs (Höganäs, Sweden).

	Ni	C	Cr	Co	W	Mo	Ta	Al	Ti	Hf	B	Zr
wt.-%	Base	0.06	8.2	9.2	9.3	0.5	3.2	5.6	0.8	1.4	0.02	0.017
At.-%	Base	0.3	9.4	9.3	3.0	0.3	1.1	12.4	1	0.5	0.11	0.011

Table 2
Process parameters of the full-factorial experiments used in this study.

Experiment	Laser power [W]	Scanning speed [mm/s]	Hatch distance [mm]
HP	125–285	600–1400	0.07–0.11
	Steps: 40	Steps: 200	Steps: 0.01
HS	205–265	3000–3600	0.02–0.035
	Steps: 20	Steps: 200	Steps: 0.005
LP	125–165	800–1100	0.05–0.07
	Steps: 20	Steps: 100	Steps: 0.01

suspension. To reveal the melt pool dimensions the samples were etched for 20 s at room temperature using aqua regia (HCl, HNO3 with a ratio of 3:1). For SEM investigations the samples were vibration polished for 8 h using oxide polishing suspension (OPS) with SiO2 < 0.05 μm. For EBSD analysis, the samples were electro polished for 15 s at 30 V using electrolyte type A2.

For microstructural examination, optical images of the specimens were acquired using a GX51 inverted microscope (Olympus K.K., Tokyo). An automated stitching method was employed, generating a comprehensive and uncompressed image of the entire XZ cross-section. Crack density analysis was conducted using the software ImageJ (Version 1.53f51). Additional microstructural analyses were performed using advanced microscopy techniques. The SEM GeminiSEM (Carl Zeiss AG, Wetzlar) equipped with an X-MarkN EDS detector and the AZtecEnergy software (Oxford Instruments, Abingdon) was utilized for the investigations. Moreover, the same SEM was employed for Electron Backscatter Diffraction (EBSD) measurements, utilizing a 60 μm aperture, a 20 kV accelerating voltage, and a NordlysNano detector (Oxford Instruments, Abingdon) with a 1 μm step size.

Microstructural characterization and phase analysis were carried out using TEM on electron-transparent cross-section samples prepared by focused ion beam (FIB) machining with a FEI Strata 400 (FEI, Eindhoven, The Netherlands). TEM investigations were performed using a 200 kV JEM-F200 microscope (JEOL, Munich, Germany). Elemental distribution maps were acquired and processed using an AZtecEnergy TEM Advanced EDX system (Oxford Instruments GmbH, Wiesbaden, Germany). Spatially resolved analysis of solute segregates at the nm scale has been carried out with APT using a CAMECA LEAP 4000X HR (CAMECA SAS, Madison). Field evaporation was assisted with thermal pulsing, employing a UV laser with 125 kHz pulse frequency. Three specimens were measured and two of the specimens exhibited premature fracture in carbides after collecting ~6 million ions at 50 pJ laser pulse energy. Therefore, a third specimen was measured with 100 pJ laser pulse energy and a yield of >100 million ions. The base temperature was 60 K and the detection rate was 0.5 % for all measurements. Data analysis was done using IVAS 3.8.8. Needle-shaped specimens were prepared by focused ion beam techniques using a FEI Helios Nanolab 660 dual-beam microscope (Thermo Fisher Scientific, Langerwehe).

High-energy synchrotron X-ray diffraction (HE-XRD) in transmission mode was carried out at the P07 beamline of the German Electron Synchrotron (DESY, Hamburg). The following experimental parameters were used: beam energy = 100 keV; wavelength = 0.124 Å; acquisition time = 5 s; sample-detector distance = 1537 mm; slit size = 0.8 × 0.8 mm^2. Complete Debye-Scherrer rings from the bulk of the sample (gauge volume = 5 × 0.8 × 0.8 mm^3) were acquired using the image plate detector PerkinElmer XRD 161 (PerkinElmer Inc. Waltham). The instrument parameters of the diffraction setup were obtained using a LaB_6 powder standard. Quantitative phase analysis of the diffraction patterns was carried out by the Rietveld method as implemented in the software MAUD (Version 2.992). An extended Williams-Imhof-Matthies-Vinel algorithm (E-WIMV) integrated in MAUD was used for texture analysis.

2.2.1. *Simulation methods*

For process simulation, a semi-analytic thermal model that resolves the part scale thermal history was employed. The conduction energy equation was solved taking the laser scan path into account. The temperatures in laser vicinity were resolved using the Eagar and Tsai model [30], while the far field temperatures are solved using a finite volume formulation capturing geometric details and environment boundary conditions [31].

Phase formation and microsegregation on the dendritic scale have been simulated using a CALPHAD-coupled multicomponent/multiphase-field model as implemented in the software MICRESS (Access e. V., Aachen) [32]. The general phase-field model is described in detail e. g. in Refs. [33–35].

For the simulations in this study, the following equations are solved:

Phase-field equations for each grain or precipitate α, expressed as the sum over all pairwise interactions αβ including triple junction terms αβγ:

$$\dot{\phi}_\alpha = \sum_{\beta}^{\check{n}} \left[M_{\alpha\beta} \left(b_{\alpha\beta}\, \Delta g_{\alpha\beta} - \sigma_{\alpha\beta} \left(K_{\alpha\beta} + A_{\alpha\beta} \right) + \sum_{\gamma}^{\check{n}} J_{\alpha\beta\gamma} \right) \right] \tag{1}$$

with: $b_{\alpha\beta} = \frac{\pi}{\eta} \left(\phi_\alpha + \phi_\beta\right) \left(\phi_\alpha \phi_\beta\right)^{0.5}$

$$K_{\alpha\beta} = \frac{1}{\check{n}} \left[\frac{\pi^2}{\eta^2} \left(\phi_\beta - \phi_\alpha\right) + \left(\nabla^2 \phi_\beta - \nabla^2 \phi_\alpha\right) \right],$$

$$J_{\alpha\beta\gamma} = \frac{1}{\check{n}} \left[\left(\frac{\pi^2}{\eta^2} \phi_\gamma + \nabla^2 \phi_\gamma \right) \cdot \left(\sigma_{\beta\gamma} - \sigma_{\alpha\gamma}\right) \right].$$

where $\check{n}$ denote the number of locally interacting phase fields. The prefactor $b_{\alpha\beta}$ represents the model-specific expression for the multiphase gradient. The thermodynamic driving force $\Delta g_{\alpha\beta}$ is calculated via the Thermo-Calc TQ-interface as function of local composition and temperature according to the quasi-equilibrium condition. The pairwise interface contributions $\sigma_{\alpha\beta} \bullet K_{\alpha\beta}$ correspond to the capillarity force, while $J_{\alpha\beta\gamma}$ account for torque forces in higher order junctions. $\sigma_{\alpha\beta}$ denotes the interfacial energy and $M_{\alpha\beta}$ the interfacial mobility. The term $A_{\alpha\beta}$ comprises higher order derivatives of $\sigma_{\alpha\beta}$ with respect to anisotropy. The interfacial mobility values are locally corrected in the thin-interface limit, according to Ref. [34], with multicomponent, multiphase correction factors evaluated from CALPHAD data.

The redistribution and diffusion of the alloying elements is described by a multicomponent diffusion equation for each element. The composition fields can be expressed in a vector notation $\vec{c}(\mathbf{x}, t)$ and map the distribution of the alloying elements during simulation. Within the diffuse interface region where adjacent phases overlap, $\vec{c}(\mathbf{x}, t)$ is defined as weighted sum of individual phase-specific compositions $\vec{c}_\alpha$:

$$\vec{c}(\mathbf{x}, t) = \Sigma_\alpha \, \phi_\alpha(\mathbf{x}, t) \; \vec{c}_\alpha(\mathbf{x}, t), \tag{2}$$

partitioning of the mixture composition $\vec{c}$ into individual phase-specific composition $\vec{c}_\alpha$ is calculated also via CALPHAD coupling, according to the quasi-equilibrium approach which postulates equal diffusion potentials $\tilde{\mu}_\alpha^i = \tilde{\mu}_\beta^i$ for each component in locally coexisting phases [36]. Diffusion is then calculated by the following diffusion equations:

$$\dot{\vec{c}}(\mathbf{x},t) = \Sigma_\alpha \nabla \cdot \vec{\mathbf{j}}_\alpha(\mathbf{x},t) + \nabla \cdot \vec{\mathbf{j}}_{atc}(\mathbf{x},t) \text{ with } \vec{\mathbf{j}}_\alpha(\mathbf{x},t) = \overline{\overline{D}}_\alpha \nabla \vec{c}_\alpha(\mathbf{x},t), \qquad (3)$$

where $\overline{\overline{D}}_\alpha$ are phase-specific diffusion matrices derived from the CALPHAD mobility database. $\vec{\mathbf{j}}_{atc}$ are multicomponent, multiphase anti-trapping terms [Carre2010], local parameter are again derived via CALPHAD coupling.

Although the model was developed to describe phase transformations close to equilibrium, it leads to valid predictions when applied to fast solidification rates associated with PBF-LB/M. This has been discussed e.g. in Refs. [37–40]. Phase-field simulations of AM processes have been reported also by other authors, e.g. Refs. [41–44].

The simulation domain had a size of $2.8 \times 2.8 \times 0.06\ \mu m^3$ with a grid resolution $\Delta x = 6.666$ nm. Periodic boundary conditions were set in the x-y-plane, adiabatic conditions on the top and bottom plane. The temperature evolution was derived from the process scale simulation, and superimposed on the domain, i.e. a frozen temperature approximation was used. From the temperature curves, only the last peak, reaching temperatures above liquidus, has been selected, i.e. re-melting or the inherent heat treatment during subsequent re-heating was not considered. The orientation of the x-y plane was set perpendicular to the dendritic growth direction with the thermal gradient in z-direction. In this configuration, the simulation domain covers a cross section of the columnar dendritic growth morphology, and the simulation describes the lateral growth of the dendrite trunks. To consider the different primary dendrite arm spacing (PDAS) for the three different process conditions, the PDAS has been determined from experimental micrographs. Then, a number of fcc-phase nuclei corresponding to the PDAS were randomly distributed at the bottom plane of the simulation domain to initiate the solidification. A deterministic nucleation algorithm was applied to nucleate secondary phases. Secondary phases of interest have been identified by thermodynamic equilibrium and Scheil-Gulliver calculations using the Thermo-Calc® software and the respective database for Ni alloys TCNI12 (Thermo-Calc Software AB, Sweden). The same database was used for phase-field simulations. The following phases were considered: liquid, γ-fcc-Ni, fcc-MC carbide, γ', μ-phase, BCC_B2, the boride MB2_C32 and the low temperature carbides M23C6, M12C and M6C. The element compositions of the precipitates are dependent on the phase equilibria during their formation and may vary during growth. Under the solidification conditions investigated in this study, the MC-carbides are mainly HfC, with up to 5 at.% Ti, Ta and Zr each. M23C6 is a Cr-carbide with a few at.% W and Mo, M6C is a carbide with W, Ni, Cr and Mo as major metallic constituents, M12C did not nucleate in any of our phase-field simulations. The MB2_C32-borides are TiB_2, BCC_B2-precipitates emerge occasionally, which are composed of Cr, Ni and Al.

Diffusion coefficients of all elements in liquid, fcc and γ' were calculated temperature- and composition-dependent from the mobility database MOBNI6 (also provided by Thermo-Calc), only considering the diagonal terms of the diffusion matrix, i.e. neglecting cross-diffusion effects for the sake of simplicity. Interface mobilities $M_{\alpha/Liq}$ for the solid/liquid interfaces were computed according to the thin interface limit, i.e. we assumed diffusion controlled growth [33], the solid/solid interface mobilities are all set to a small value of 10^{-9} cm^4/J, practically disabling the movement of solid/solid interfaces on the time scale of solidification which is a physically reasonable approximation. Interfacial energies $\sigma_{\alpha\beta\bullet}$are all set to $1.5 \cdot 10^{-5} J/cm^2$. It is a typically value and has been used to simplify the parameter selection. In this study, the comparison between different cooling rates is addressed which is not affected by differences in interfacial energies.

3. Results

3.1. Experimental investigations in as built CM247LC

3.1.1. Process parameter variation in PBF-LB/M CM247LC

Fig. 1 a) displays the resulting crack densities, along with their corresponding linear energy inputs. The linear energy was calculated by dividing the laser power P [W] by the scanning speed v [mm/s]. Therefore, a decrease in P or an increase in v leads to lower linear energy. The polynomial fitting curve exhibits a clear trend, indicating that crack density decreases with lower linear energy. Fig. 1 b) shows that low linear energy correlates with formation of wide, shallow melt pools, which are characterized by an aspect ratio <0.5 $\left(\frac{\text{Meltpool depth}}{\text{Meltpool width}}\right)$. These melt pools are primarily formed through conduction mode welding. In contrast, high linear energy results in higher aspect ratios and deep, narrow melt pools are formed, corresponding to a capillary dominant welding regime. This welding regime appears to be associated with a higher ratio of observed cracks in the micrographs.

Table 3 presents three process parameter sets chosen from the DOE analysis (indicated in red colour in Fig. 1). These parameter sets are chosen based on the lowest crack density for the three conditions high power (HP), high speed (HS) and low power (LP). LP and HS result in comparably low crack densities, while HP has a high crack density.

3.1.2. Microstructural characterisation

Fig. 2a–c display cross-sections of the cubic samples providing a characterization of the microstructure and associated defects in the as-built state. Examination by light optical microscopy revealed the presence of defects such as cracks (indicated by grey arrows), pores (indicated by red arrows), LoF defects (indicated by black arrows) and balling defects (indicated by green arrows), which are distributed throughout the samples. Most cracks are aligned parallel to the building direction (BD). SEM images were taken from the central region of the specimen. In all states, a typical cellular-dendritic structure is observed. In HP (Fig. 2 d), the orientation of the dendrites is distributed at different angles to the building direction. Cracks with a length of up to several hundred μm are recognizable. The alignment of the dendrites to the build direction increases strongly in HS (Fig. 2 e) and especially in LP (Fig. 2 f). In LP (Fig. 2 f), numerous dendrites can be seen cut in parallel with only a slight misorientation towards the building direction. In addition, melt pool boundaries can be found at Fig. 2 e) and **f)**, highlighted by white arrows. SEM-EBSD was performed to investigate the relation between process parameters and grain size, morphology and orientation texture of CM247LC. The orientation mappings regarding the building direction are shown in Fig. 2g–i. Additionally for each experiment, an inverse pole figure (IPF) with respect to the building direction is provided. HP and DP show a predominant texture of the [001] component towards the building direction. The grains of LP are columnar and orientated parallel to the building direction. The length spans over several hundred μm and exceeds the measured area. HS shows thinner, elongated grains, that are tilted towards the inert gas flow direction. The primary textural component of [001] is less pronounced.

Fig. 3 shows the SEM images of several defects in the as-built samples. Fig. 3 a) presents an indication for liquation cracking alongside a circular phase with an approximate diameter of 3 μm, which is further highlighted in Fig. 3 e). Subsequent chemical analysis via SEM-EDS confirms the phase as precipitate that is rich in Hf (Appendix 1). The size of these particles indicates that they could not form during solidification within the dendritic mushy zone. Instead it is likely that they are unmolten HfC-precipitates originating from the powder feedstock. Fig. 3 e) shows the presence of white, smaller phases within the interdendritic spacing. Fig. 3 b) and **f)** show the presence of dendritic protrusions within an open crack surface. This observation serves as an indication that the crack formation was facilitated in the presence of a liquid phase, thus categorizing the crack as SC. In Fig. 3 c) spherical defects with

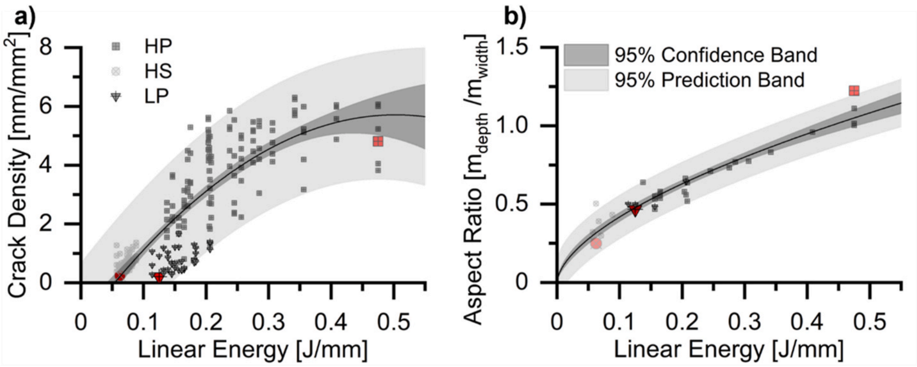

Fig. 1. Results of the conducted experiments. Specimens used for further investigations are marked in red. a) Correlation of crack density with the corresponding linear energy input. An increase in linear energy leads to an increase of crack density. b) Correlation of the resulting aspect ratio of the melt pool geometries with the corresponding linear energy input. The aspect ratio increases with increasing linear energy.

Table 3
Parameters of three distinct states of process conditions, as indicated in red colour in Fig. 1 and used for further analysis. Specimens processed with parameters in HS and LP achieve the lowest crack density whereas those processed in HP reveal significantly higher crack density.

Experiment	Laser power	Scanning speed	Hatch distance	Linear energy	Crack density	Aspect ratio
	[W]	[mm/s]	[mm]	[J/mm]	[mm/mm^2]	[m$_{depth}$/m$_{width}$]
HP	285	600	0.07	0.48	4.81	1.22
HS	225	3600	0.02	0.06	0.25	0.25
LP	125	1000	0.05	0.13	0.21	0.47

larger dendritic structures are found in the HS samples. The development of a coarser dendritic structure may arise because the insufficient bonding to the underlying layers leads to a constrained heat dissipation of the defect and therefore to locally lower cooling rates. Notably, these defects appear to serve as initial sites for the onset of crack propagation. Fig. 3 g) offers an internal view of one of these defects, revealing the presence of precipitates exhibiting a complex morphology. Fig. 3 h) shows a crack that is comparably straighter in appearance.

Fig. 4 a) – b) shows a TEM bright-field (TEM-BF) image of various solidification cells with a distinct contrast between the cells, as seen in Fig. 4 a). These cells stem from the columnar dendritic growth morphology pointing perpendicular to the image plane shown here. The element enrichment in the intercellular regions leads to the formation of precipitates, represented by black dots. A high dislocation density is visible as well. Fig. 4 b) show precipitates that are rather spherical with a size of about 40–80 nm. A total of 35 spectral analyses showed an increased amount of C, Cr, Ti, Hf, Ta and W, with only few indications for Mo, Al and Zr, which is summarized in Appendix 2. For further identification of phases, TEM-SAED were conducted. Fig. 4 c) shows the diffraction patterns with the marked reflections of the disordered γ-phase (Fm-3m, Cu-type) as well as the ordered γ′-phase (Pm-3m, AuCu3-type). The lattice parameter of the γ′-phase is calculated as a = 3.62 Å, which is in good agreement with the literature value of a = 3.59 Å for γ′-$AlNi_3$ in IN738LC [45], thus indicating the existence of the γ′-phase in as built CM247LC. Note that there has been no significant difference in the intensity of reflections between intercellular and dendrite core areas. Fig. 4 d) – k) shows TEM-EDS maps displaying the elemental distribution on the scale of the solidification cells. The cells, corresponding to the dendrite spacing, have a diameter of approximately 0.5–1 μm. Notably, several precipitates are visible as black dots on the borders of these cells, showing enrichment in elements such as C, Hf, Ta, Ti, W (Fig. 4f–h, i, j, k). Intercellular regions are enriched in Al, Hf, Ti (Fig. 4e–h, j). The findings are in agreement with results from literature [12,21].

To further elaborate the elemental distribution APT measurements were conducted to provide a nano-scale resolution on the local enrichment of Al and Cr as well as carbides, borides and their surroundings. The reconstruction of a specimen with a length of approximately 800 nm is shown in Fig. 5 a) and Cr as well as Al enrichment is evident in the distance range of 30–120 nm. The composition profile reveals that the measured matrix composition is in good agreement with the nominal composition (Table 1). Moreover, the Ni and Co contents are locally depleted to <1 at.% at a distance of 71 nm, while the Cr and Al contents correspond to a ratio of Cr_3Al and chemical ordering has been observed for this composition [46]. In the distance range of 76–86 nm an Al-rich region is found with 41 ± 4 at.% Al. Another region of the atom probe reconstruction is magnified in Fig. 5 b). The composition profiles emphasize the formation of Al-rich regions at a distance of 470 nm and 588–590 nm. also shows a Hf concentration above 5 at.%. This significant Ti enrichment, and to a lesser extent that of Hf, agree with the intercellular segregation observed in the TEM data. Enrichment of the heavier metals can be observed at 473 nm and a mixed carbide is detected at a distance of 485 nm. Moreover, the formation of a boride is evident in a distance range of 563–567 nm. Finally, an indication for local γ′ formation is found at 578 nm consistent with Ni_3Al.

Two further APT examinations were carried out, which were terminated by specimen fracture within carbides. These investigations supported the existence of MC mixed carbides (including Cr, Hf, Ni, Ta, Ti and W) as well as WC carbides. The results can be seen in Appendix 3.

HE-XRD was performed to compare the phase fractions of MC-carbides and γ′ in correlation to the processing parameters. Five specimens representing the HP, LP, and HS conditions have been measured. Fig. 6 shows the intensity peaks with the corresponding 2-θ-angles. Owing to the low volume fractions (<1 vol%) and the small size of the phases (few nm), only a qualitative comparison of the phase fractions is possible. However, notable observations were made. The peaks corresponding to MC-carbides and γ′-phase exhibit lower intensities for the HS and LP samples, as compared to the three HP samples. This observation points into the direction that the number of MC-carbides is larger for lower cooling rates.

3.2. Numerical assessment

As illustrated in Fig. 1, a noticeable correlation is evident between a reduced linear energy input, leading to shallower and broader melt pools, and a concurrent decrease in crack density. To gain deeper insights into inherent thermal conditions, HP, HS and LP are simulated as single layers of the process and relevant metrics were analysed. Fig. 7 a) presents a simulated layer of the process, accompanied by the corresponding melt pool dimensions in Fig. 7 c). Fig. 7 b) provides the extracted time-temperature charts for the three specimens: HP, HS, and LP.

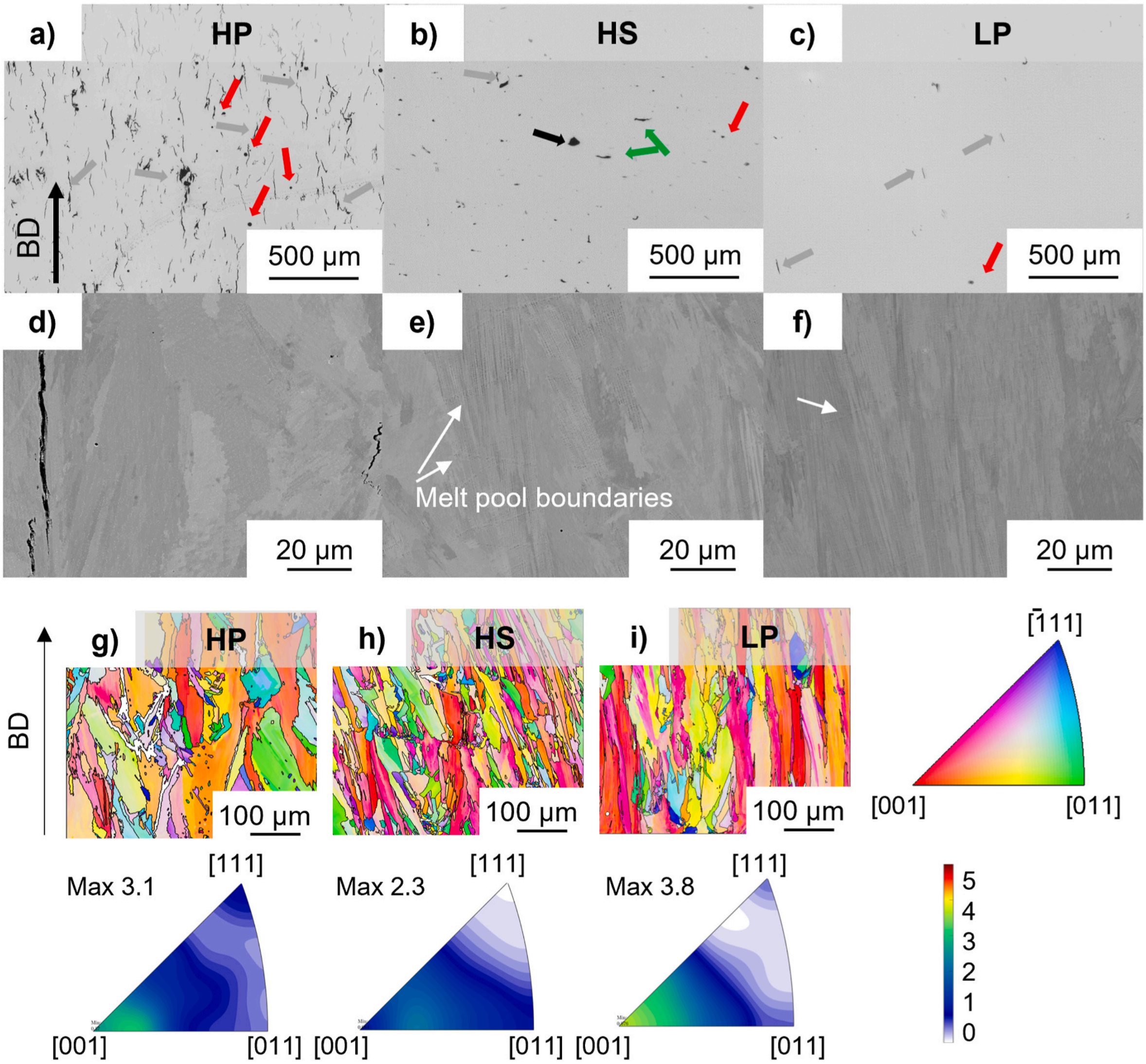

Fig. 2. Representative micrographs illustrating defects present in as-built CM247LC. Pores, LoF defects, balling defects and cracks are indicated by red, black, green and grey arrows, respectively for HP (a), HS (b), LP (c); SEM micrographs of polished samples to investigate the solidification structure for HP (d), HS (e), LP (f); inverse pole figure (IPF) mappings ([001] parallel to BD) to investigate the size and orientation of grains for the respective samples HP (g), HS (h) and LP (i).

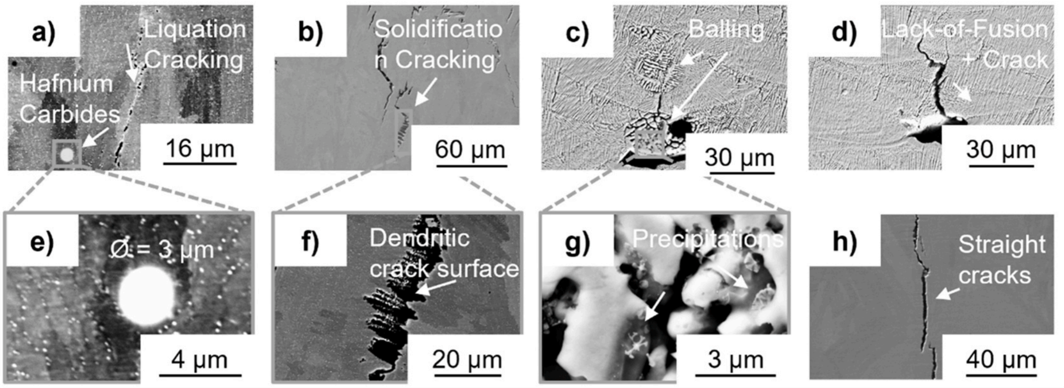

Fig. 3. SEM secondary electron micrographs of a, e) liquation cracking and Hf-carbide; b, f) solidification cracking; HS: c, g) balling defects and carbides; LP: d) LoF and crack initiation; h) straight crack.

As expected, the highest linear energy of HP results in the largest melt pool dimensions with the lowest cooling rate of 65,000 K/s compared to 570,000 K/s for LP. The melt pool volume is 0.09 mm^3, which is nine times higher than that of the other parameters HS and LP with 0.01 mm^3. While resulting in comparable melt pool dimensions, the higher scanning speed in HS and the lower laser power in LP results in

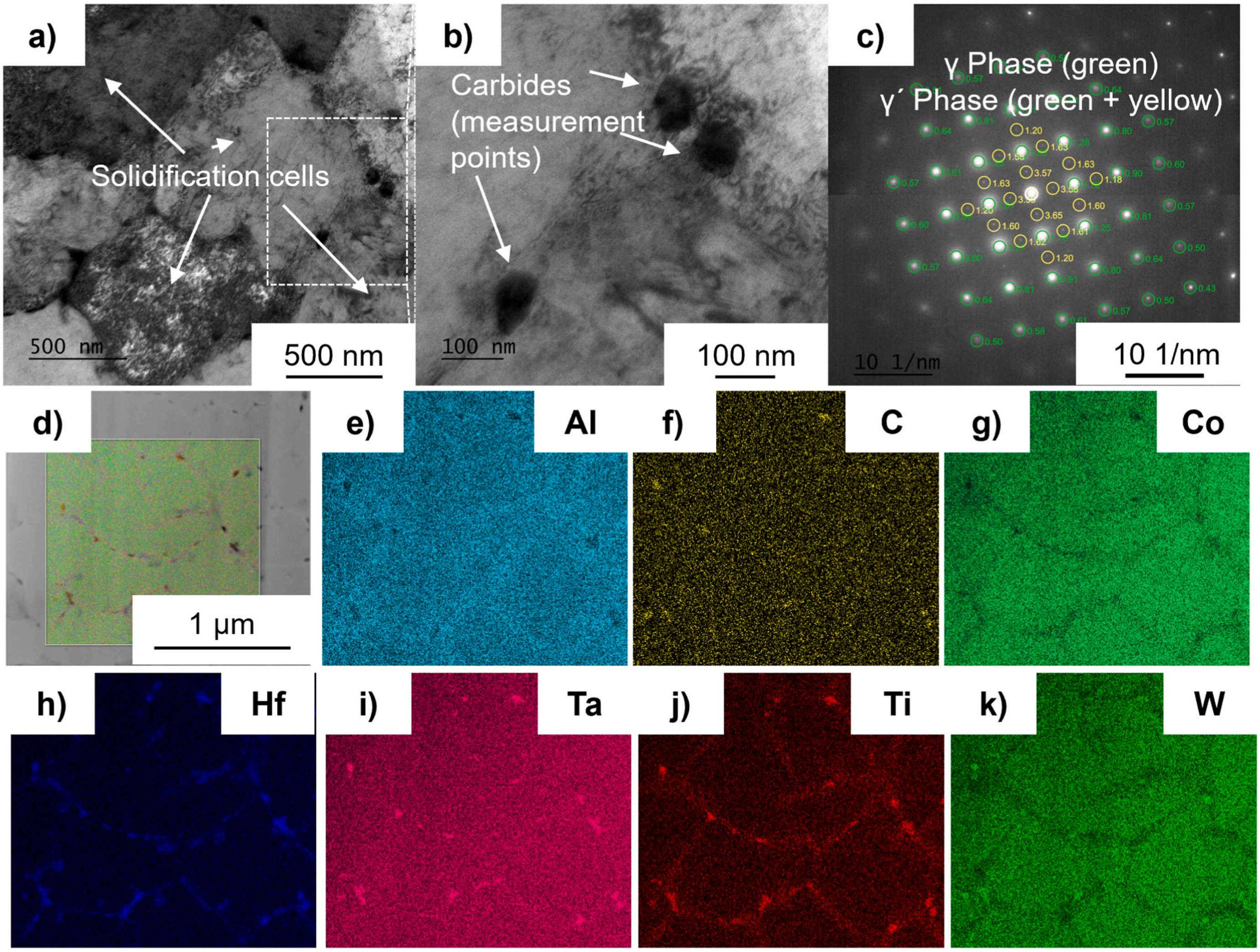

Fig. 4. TEM analysis of the LP state. a) TEM-BF image showing a high dislocation density and solidification cells; b) carbides at intercellular regions; c) TEM-SAD patterns of the sample with diffraction spots indicating the γ-phase/γ′-phase are encircled in green/yellow respectively; d) TEM image showing the investigated solidification cells; e-k) TEM-EDS elemental distribution maps of the respective elements.

shallower and thinner melt pools, see Table 4.

The phase-field simulations provide quantitative data for the evolution of the phase fractions. In Fig. 8, the phase fractions, integrated over the simulation domain, for the solid phases γ and γ′, MC and M23C6 carbides, borides, μ-phase and the bcc-phase are plotted over temperature for all three process conditions. M6C and M12C carbides are also predicted by the simulations, but in amounts less than 10^{-6} which makes it unlikely that they are seen in the experimental micrographs.

MC-carbides are the second solid phase after the primary γ-fcc to form. These carbides become stable around 1587 K corresponding to 17 % residual liquid, followed by boride formation around 1563 K at 12 % liquid. This explains that the precipitates are found in the interdendritic channels and exhibit sizes in the range between 10 nm and 100 nm. They are growing from the melt which enables diffusion over longer distances (a few μm in 0.1 ms) compared to the solid state. The next phase to form is γ′, which becomes stable in the solidification interval according to the thermodynamic data and thus, can also grow from the melt. In the TEM and SEM investigations larger primary γ′-particles were not observed. Possible reasons for this discrepancy are e.g. minor deviations in the Gibbs energies provided by the database or a higher nucleation barrier for the formation of γ’.

Fig. 9 shows the simulated, as-solidified structure for the three different process parameters. Areas with the ordered γ′-phase are located in triple line regions. The γ′-phase is growing from the melt and forms larger particles compared to the secondary γ′-precipitates that emerge by solid state precipitation. As stated above, the different solidification cell sizes correspond to the different PDAS identified from the experimental observations and have been predefined by the number of γ nuclei.

Table 5 comprises the volume fractions and particle sizes of MC-carbides, borides and γ′ as derived from the simulation. A trend can be seen for the amount and size of the MC-carbides. With increasing cooling rate, from high-energy (HP) to low-power process parameters (LP), the integral volume fraction, size and volume density of MC-carbides decreases, e.g. the integral volume fraction by about a factor of 10. Furthermore, the simulations show only a little decrease of the volume fraction of borides with increasing cooling rate, whereas the γ′-fraction is increasing. The size of borides is slightly smaller than those of the MC-carbides, the particle density is around 100 precipitates per μm^3. The volume fraction of γ′ is the highest in LP condition with 7.79 vol%, while HP and LP show volume fractions of 5.66 vol% and 7.55 vol%, respectively. Here, it must be noted that due to the stochastic nature of the nucleation, in experiments as well as in the simulation, a parameter study with a larger amount of samples or simulations would be necessary to achieve statistically robust results. Also, the choice for the semi-empirical parameters of the nucleation model need a more detailed investigation. In this study, the model parameters have been calibrated

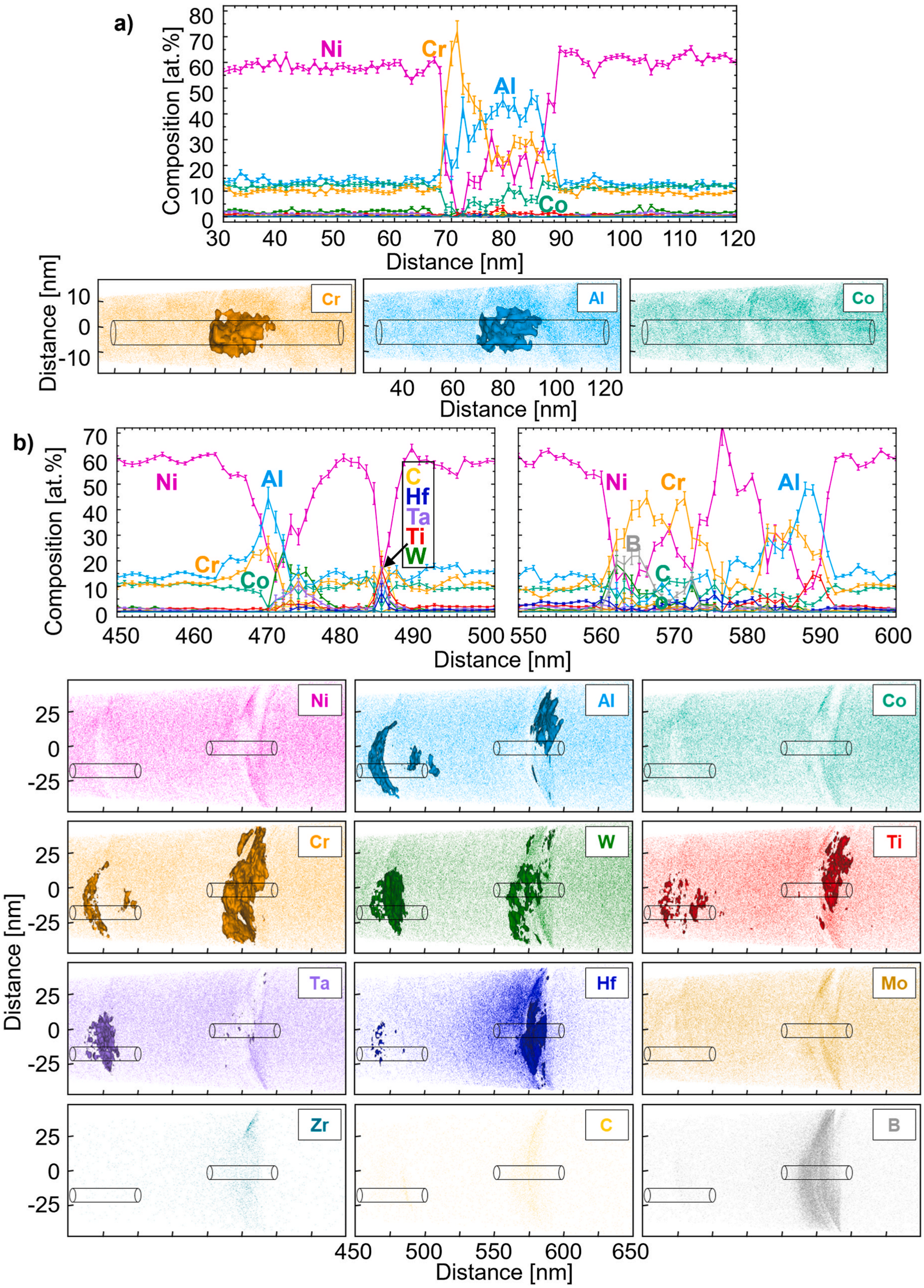

Fig. 5. a) APT analysis of an Al-rich region with reconstruction of atomic positions of Al, Co and Cr in the distance range from 25 to 125 nm and isoconcentration surfaces emphasize Al-rich (≥35 at.%) and Cr-rich (≥25 at.%) regions, **b)** APT analysis of Al-rich as well as B- and C-rich regions with reconstruction of atomic positions of Ni, Al, Co, Cr, W, Ti, Ta, Hf, Mo, Zr, C and B in the distance range from 450 to 650 nm and isoconcentration surfaces marking Al-rich (≥35 at.%), Cr-rich (≥25 at.%), W-rich (≥10 at.%), Ti-rich (≥6 at.%), Ta-rich (≥8 at.%) and Hf-rich (≥10 at.%) regions. c) Composition profiles from the cylindrical regions in the distance range from 450 to 500 nm and from 550 to 600 nm, regions are indicated in b).

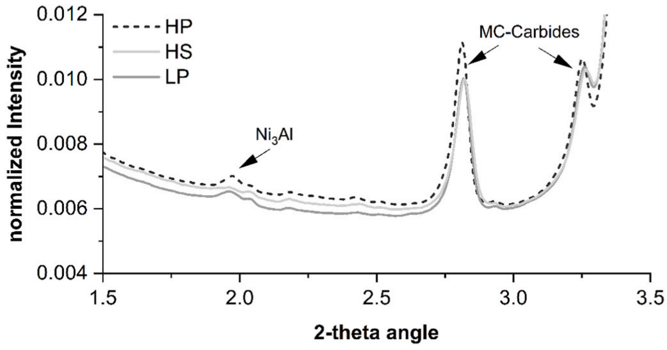

Fig. 6. Normalized diffraction intensities for five specimens as a function of 2-theta angles. Intensity peaks for γ′ as well as MC-carbides are the lowest for HS, followed by LP and HP.

to match the experimental observations qualitatively. The typical size of the simulated MC-carbides in the range between 20 and 40 nm is comparable to the experimentally observed values (40–80 nm) for LP (Fig. 5). Furthermore, the nucleation model parameters are kept constant in order to elucidate the effect of different cooling rates. The simulated trend for the MC-carbide formation agrees with the observed trend in the experimental results, e.g. those from HE-XRD (Fig. 6).

As described in **3.2.2.**, the thermal conditions from process scale simulations are taken as boundary conditions for the microstructure simulations using the multiphase-field method. Fig. 10 shows the simulated distribution of the alloying elements, comparable to the TEM-EDS mappings for process conditions LP. Punctual enrichments can be observed in the intercellular regions for the elements C, Hf, Ta, Ti, W (Fig. 10c–f, i, j, k, l), and to a lesser extent, for Mo and Zr (Fig. 10g and h), indicating the formation of carbides. Additionally, the punctual enrichments of B (Fig. 10 l) are related to borides in the intercellular regions. Segregation bands in intercellular regions are observed for Al, Hf, Ti (Fig. 10b–f, j), and to a lesser extent for Cr and Mo (Fig. 10e–g).

Fig. 11 shows another simulation example for the segregation behaviour of Mo, Ta and W in the last stages of solidification (cut out from the simulation box). The times are chosen such that t = x ms represents the start of phase formation in the interdendritic space, while x+2.4 ms represents the time at which the residual melt has completely solidified. Mo is showing a relatively weak enrichment in the residual liquid and consequently an associated enrichment of about 1–1.5 at.% in the solidified melt fringe after complete solidification. The small concentration differences could explain the missing indication from the TEM element mapping. A similar behaviour is found for Cr. In contrast, Ta and W are predominantly bound in precipitates located in the intercellular space. In the case of Ta, the intercellular regions seem to be enriched, while in fact, Ta is mainly enriched in γ' and carbides. W is depleted in the intercellular regions, while it shows high concentrations up to 30 at.% within MC-carbides.

The following Tables 6 and 7 summarize the experimental observations regarding phase formation and element distribution on the dendritic length scale, i.e. microsegregation, and provide a semi-quantitative comparison with the simulation results. The symbol + indicates an enrichment of the elements in the corresponding analysis method, while (+) indicates a weakly pronounced enrichment. A distinction is made between the enrichment of elements in the cell cores and cell boundaries (Table 6), and also for elements that are identified in

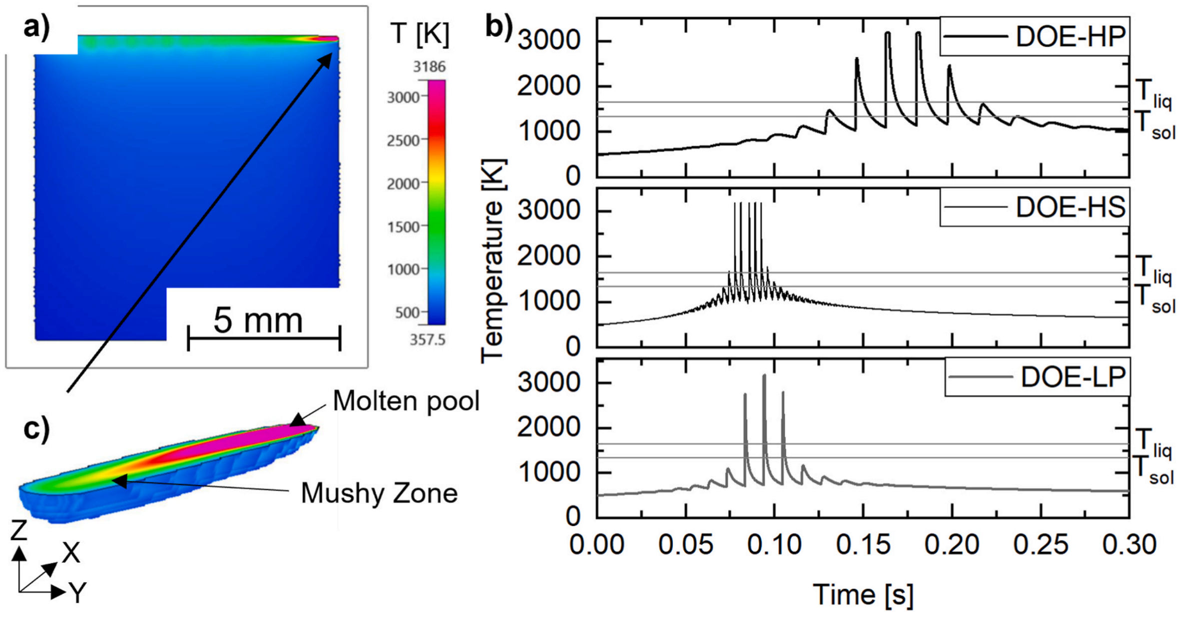

Fig. 7. Process simulation of a single PBF-LB/M layer. a) thermal field for a hatch trajectory of one layer; b) time-temperature charts for a fixed point within the grid for HP, HS and LP; c) extracted simulated melt pool with respective temperature distribution.

Table 4
Extracted metrics from the process simulation for the three cases: HP, HS and LP.

Experiment	Simulation						
	Linear energy	Melt pool dimensions depth | width | length			Melt pool volume	Cooling rate	Quantity of complete fusions
	[J/mm]	[μm]			[mm^3]	[K/s]	
HP	0.48	206	265	1471	0.09	65,000	4
HS	0.06	36	123	1067	0.01	350,000	7
LP	0.13	65	129	642	0.01	570,000	3

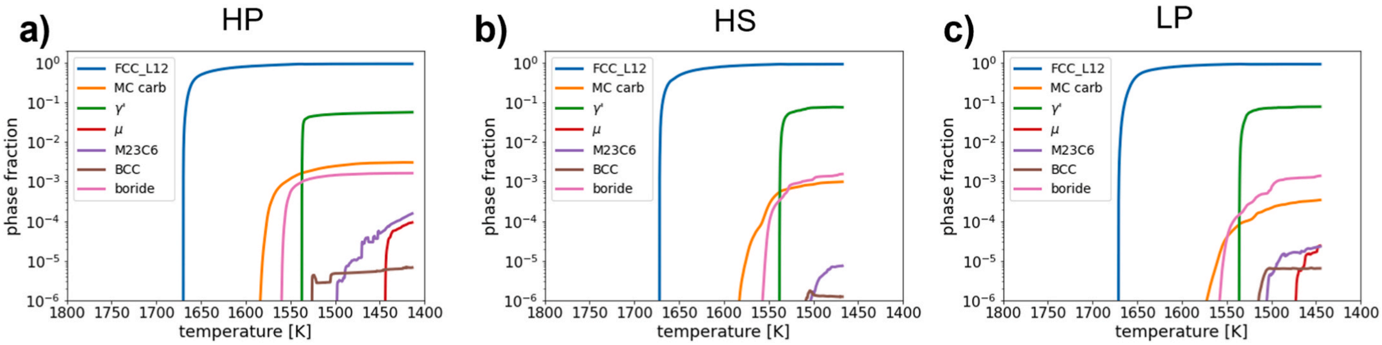

Fig. 8. Comparison of the evolution of phase fractions over temperature for a) HP, b) HS and c) LP, respectively.

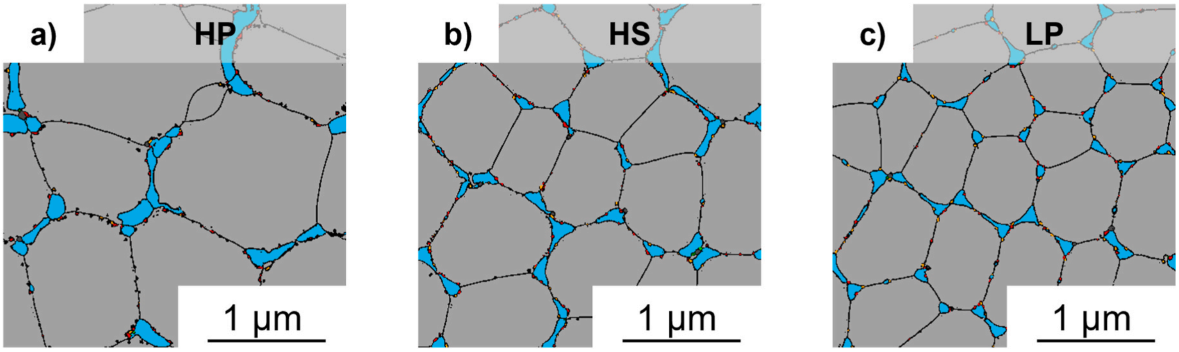

Fig. 9. Simulated phase distribution for the different process parameters: a) HP, b) HS and c) LP. With liquid: dark grey, fcc-Ni/γ: light grey, MC-carbides: red, borides: orange and γ': light blue."

Table 5
Quantity and size of MC-carbides, borides and γ′ for the parameters HP, HS and LP.

		HP	HS	LP
MC-carbides	vol%	0.3	0.1	0.034
	Typical Ø [nm]	50–80	25–40	20–40
	Density [μm^{-3}]	200	88	60
Borides	vol%	0.16	0.15	0.14
	Typical Ø [nm]	25–50	25–40	25–35
	Density [μm^{-3}]	102	106	108
γ'	vol%	5.66	7.55	7.79
	Avg. Ø [nm]	142.4	134.7	111.8

the precipitates (Table 7).

As Table 6, all three investigation methods show intercellular regions enriched in Cr, Ti, Al and Hf. This is in accordance with literature, e.g. Refs. [12,47]. Heavier elements, such as Mo, Ta and W are partly enriched in the intercellular regions and are experimentally identified only by the APT measurements, while the TEM element mapping shows no indications.

Table 7 compares the detected elements in regions that are assigned to precipitates, as derived from the experimental data. While some phase constituents may differ, the basic conclusions about phase formation and composition between experiment and simulation is that they agree qualitatively well showing MC-carbides of different compositions, γ' and borides in as-built condition. As primarily indicated by the TEM measurements, the APT and simulation results confirm MC-carbides mainly consisting of C, W, Ti, Ta and Hf, indicated by the yellow colour filling in Table 7. Mo and Zr are only slightly enriched, as confirmed by simulations showing 0.64 at.% Mo and 0.14 at.% Zr.

4. Discussion

In this study, the correlation between process parameters and resulting microstructure with focus on defects is investigated, both experimentally and by numerical simulations. The different process parameter combinations affect the melt pool formation and solidification conditions, and, thus, element segregation, phase formation and grain morphology. Through a vast parameter study, parameter sets where identified, which result in a low cracking density, which could, yet, not be achieved in current literature. The experimental results indicate that the linear energy has the strongest effect on the mentioned microstructural features. Furthermore, the grain morphology and texture cannot be directly correlated to the cracking behaviour of CM247LC, which contradicts current literature.

4.1. Influence of process parameters on cracking susceptibility during solidification

The cracking susceptibility of CM247LC in PBF-LB/M is strongly correlated with the process parameters. Whereas individual process parameters, e.g. scanning speed, alone do not show a good correlation with the crack density, the calculated linear energy correlates well with the crack density of the samples as shown in Fig. 1. This underlines the findings by Fardan et al. [20], which first showed this correlation on multiple samples. The difference in cracking behaviour can be explained e.g. by a larger mushy zone in the samples with a higher linear energy. Based on the hot cracking criterion by Rappaz et al. [48], a large mushy zone supports solidification cracking due to isolation of areas without liquid feeding in combination with the thermal contractions resulting from solidification. The increase of mushy zone in CM247LC with increasing linear energy is already shown through a combination of temperature field calculations and CALPHAD simulation by Ref. [20]. Furthermore, the findings in Fig. 1 also show a strong correlation

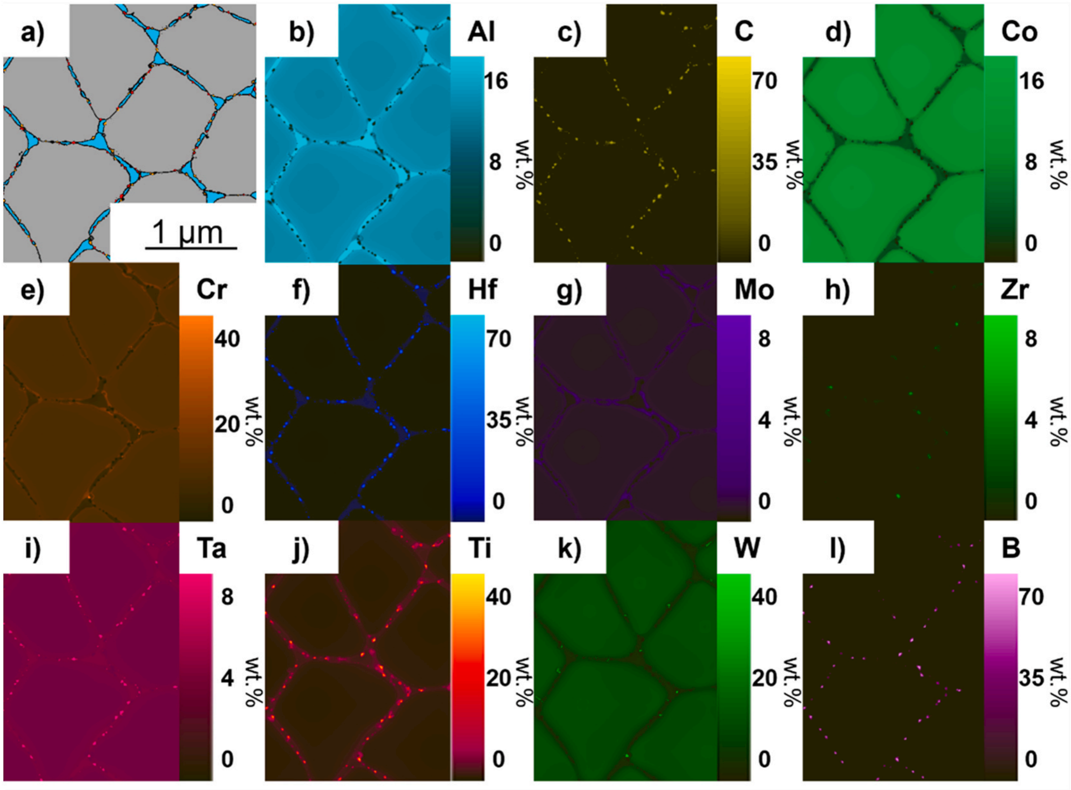

Fig. 10. Representation of the simulated element distribution in the solidification cells for LP. a) Simulated phase distribution, b-l) element distribution with manually adjusted colour scales to mimic TEM-EDS element mappings. A quantitative analysis of the element concentrations is following later on.

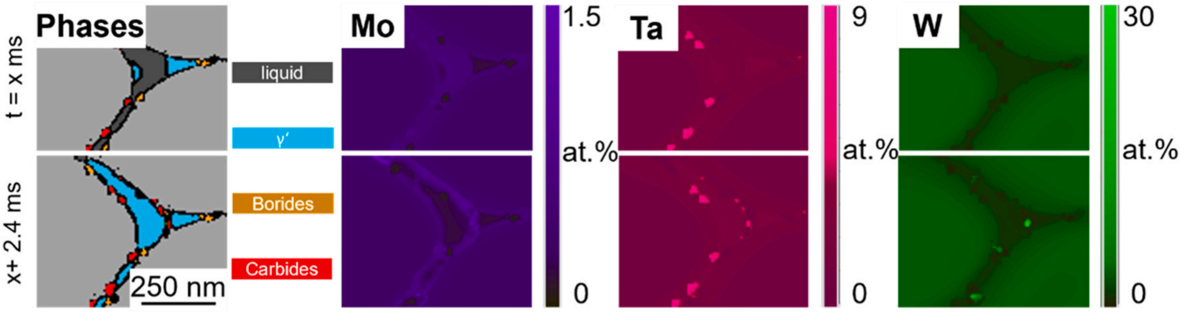

Fig. 11. Simulated phases and corresponding Mo, Ta and W distribution. t = x ms represents the start of phase formation in the interdendritic space, while x+2.4 ms represents the time at which the residual melt has completely solidified. Mo enriches in the residual liquid, while Ta and W are bound in γ′ and MC-carbides.

Table 6
Comparison of the intercellular enrichment of elements (without the presence of phases other than γ) in LP condition as obtained by TEM-EDS, APT, simulation. The symbol "+" indicates the enrichment of an element and (+) a lower indication for an enrichment. A green background shows an agreement between the evaluation methods. A red background showcases discrepancies.

Comparison of observed intercellular segregation												
Method	Ni	C	Cr	Co	Mo	W	Ti	Al	Ta	Hf	Zr	B
TEM-EDS			(+)				+	+		+		
APT			+		(+)	(+)	+	+	(+)	(+)		
Simulation			(+)		(+)		+	+		+		
Validation			✓		✓	✗	✓	✓	✗	✓		

Table 7
Phase formation for the respective investigations with cell colouring for carbides (yellow), borides (red), γ' (light blue) and Cr_3Al (dark blue, from APT).

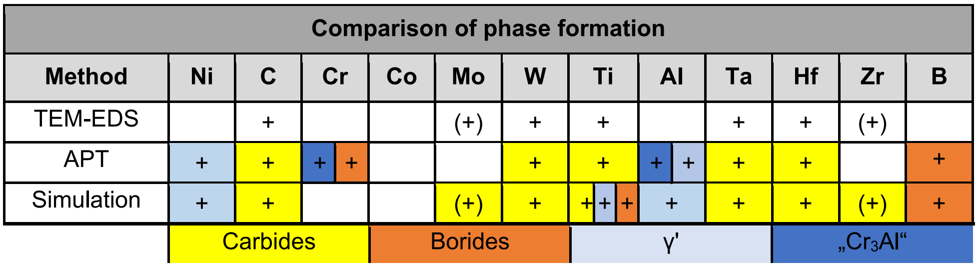

Comparison of phase formation												
Method	**Ni**	**C**	**Cr**	**Co**	**Mo**	**W**	**Ti**	**Al**	**Ta**	**Hf**	**Zr**	**B**
TEM-EDS		+			(+)	+	+		+	+	(+)	
APT	+	+	+ +			+	+	+ +	+	+		+
Simulation	+	+			(+)	+	+ + +	+	+	+	(+)	+

Carbides Borides γ' „Cr_3Al“

between the aspect ratio of the melt pool and the crack density. The shallower the melt pool, the less cracking appears. Shallower melt pools result in less cyclic remelting and reheating in build direction. On the one hand, reheating could lead to a reduction of residual stresses [1] and crack healing through remelting [49], on the other hand it increases the risk for liquation cracking in the heat-affected-zone (HAZ) surrounding the molten tracks [50,51], and impacts the precipitation formation and distribution of phases [52,53]. These findings are contrary to Ref. [20], where narrow melt pools were argued to have a positive influence on the cracking susceptibility. One possible reason for this discrepancy could be the bias of a small quantity of investigated process parameters, compared to the vast number of parameter combinations in this study.

A correlation of grain morphology and texture with the crack density could not be found. The results in Fig. 2 show a strong epitaxy in the LP sample with the strongest texture in [001] direction and, contrary, the lowest crack density. In current literature, the impact of epitaxy and resulting high amount of high-angle grain boundaries (HAGBs) is described as strongly correlated to cracking, since solidification cracking occurs almost exclusively at HAGBs (e.g. Ref. [26]). It can be argued, that by achieving similar grain sizes, the amount of HAGBs influences the cracking behaviour, but for completely different states with different grain sizes, as characterized in this study, the correlation could not be drawn.

In the following, the effect of different cooling rates on the resulting segregation and phase formation during solidification is discussed as a potential cause for the different cracking behaviour observed in the three representative samples build with HP, HS and LP process parameters.

4.2. Validation of simulated cooling rate and melt pool dimensions

In Table 8 the simulated melt pool dimensions are shown together with simulated cooling rates and measured primary dendrite arm spacing. The simulated melt pool widths are in good agreement with the experimentally observed melt pool widths, with a maximum deviation of less than 10 %. The depths of the melt pools show a good match for the two samples HS and LP, where the conduction welding regime is dominant. The simulation of the capillary dominant melt pool regime of HP leads to an underestimation of the melt pool depth of 206 μm instead of 352 μm.

Table 8
Derived metrics from the process simulation in comparison to measured data.

Experiment	Measured data			Simulation	
	Linear energy	PDAS	Melt pool dimensions (depth/width)		Cooling rate
	[J/mm]	[μm]	[μm]	[μm]	[K/s]
HP	0.48	1.27	352/288	206/265	65,000
HS	0.06	0.73	32/129	36/123	350,000
LP	0.13	0.61	65/139	65/129	570,000

Investigations on the primary dendrite arm spacing (PDAS) show a consistent trend compared to the simulated cooling rates, i.e. faster cooling results in a finer dendritic solidification structure with smaller PDAS. Various publications cite a source in which the empirical scaling law for the relationship between dendrite arm spacing and cooling rate for nickel-based superalloys is described [54,55], as seen in Equation (1). The given material constants correlate well with our results.

$$d = a\varepsilon^{-b} \tag{4}$$

where a and b are material constants equal to a = 50 μm*K/s and b = 1/3 for nickel-based superalloys. The parameter d is the PDAS, while ε is cooling rate [56,57]. The formula gives a cooling rate for HP of about 61,000 K/s, 320,000 K/s for HS and 550,000 K/s for LP. Remarkably, these values closely align with the previously calculated cooling rates from the process simulation, displaying a maximum deviation of less than 10 %. The consistency of the measured PDAS and the simulated cooling rates in terms of the scaling law can be seen as evidence for a reliable prediction of the cooling rate by the process simulations. Various studies deal with the correlation of the cooling rate and segregation phenomena during solidification [58–62]. Another factor worth noting is the low hatch distance of HS, resulting in multiple instances of remelting of up to seven times. In comparison, HP and LP involve material remelting four and three times, respectively. By that means, the material is experiencing several solid-state heating cycles with decreasing intensity and possible heat accumulation in the part. As already discussed, this can increase the risk of liquation cracking and impacts the precipitation and distribution of phases.

4.3. Phase formation and micro segregation

Experimentally, the presence of γ'-precipitates was confirmed through TEM-SAD (Fig. 4) and further verified by HE-XRD (Fig. 6). Complementary, APT showed an indication for Ni_3Al in Fig. 5. Literature also confirms the presence of nanoclusters of γ' in PBF-LB/M-processed CM247LC in as-solidified condition [21,63,64]. Simulation results indicate the existence of substantial amounts of over 5 vol% of γ'-phase emerging in the last part of the solidification path, consequently located in the intercellular regions, while no γ' is formed within the cell core. Contrary to the simulation results, the diffraction patterns of TEM-SAD showed no significant difference in intensity comparing the cell cores and cell boundaries. APT measurements on the other hand showed an indication for local γ' formation in Fig. 5 in the intercellular regions, while the HE-XRD results indicate that the volume fraction of these precipitates is less than 1 vol%. However, the high content of Al and Ti up to 48 ± 3 at.% Al, and up to 15 ± 1 at.% Ti (Fig. 5) in the intercellular space detected by ATP could be an indication for the formation of primary γ'-phase during solidification.

Moreover, simulation revealed the presence of borides (0.16 vol%) in the intercellular regions. These borides are predominantly composed of Ti and B (TiB_2) and exhibit diameters in the range of 25 nm–50 nm. APT investigations confirmed the presence of nanoclusters of borides in as-built PBF-LB/M condition, with an enrichment of Cr. Despite that observation, XRD analysis from literature showed no evidence of borides in as-built PBF-LB/M-CM247LC [64], while being proven in as-cast CM247LC [65]. The APT measurement in Fig. 5 is showing an indication for Cr_3Al. Particles or phases with this composition are not predicted by the simulation nor found elsewhere in literature for this alloy. The BCC appearing in the simulations shows an Al composition between 25 and 30 at%, but instead of 75 % Cr, it is dominated by Ni with a few % of Cr and other substitutional elements. In addition to that, the simulation results showed the formation of the μ-phase (0.017 vol%) primarily consisting of Cr, W, along with minor contributions of Mo, Ti, Al and Zr. Moreover, $M_{23}C_6$-carbides (0.0013 vol%) were observed, characterized by constituents such as C, Cr, Mo, Ti and Zr. However, due to the limited volumetric proportions of these phases, an experimental analysis was not pursued.

As shown e.g. in Fig. 8, the phase-field simulations show several differences in the phase formation and segregation behaviour for the three different processing conditions HP, HS and LP. To further illustrate the phase formation of γ‘, MC and borides, Fig. 12 shows examples of the microstructure simulations in different levels of detail for the LP state. In Fig. 12 a) the initial growth of fcc-dendrites solidifying from the melt is shown. Temperature gradient and the primary dendrite growth direction are perpendicular to the 2D slices shown in the figures. Fig. 12 b) shows the coalescence of the dendrites and the associated formation of liquid channels in between. At this point (t = 1.6 ms), the first carbides are already nucleated in the melt, see cutout in Fig. 12 c). A few ms later (at t = 2 ms), borides and γ’ begin to form (see Fig. 12 d)). Fig. 12 e) shows a cutout from the solidified structure. The intercellular space is filled with secondary phases, mostly γ’ plus carbides and borides.

Phase formation towards the end of solidification has two main potential effects on hot cracking. Firstly, it governs the solidification interval, i.e. the termination of the solidification is governed by the phase formation in the residual melt, highly enriched in alloying elements. Different hot cracking models suggest a direct correlation between the solidification interval and the hot cracking susceptibility of an alloy. Secondly, precipitate formation can promote the coalescence of neighbouring dendrites or even building a mechanical bridge between them. This will enhance the mechanical stability of the mushy zone.

Size and quantity of precipitates depend on the cooling rate and consequently, the cooling rate should affect the crack density in CM247LC. When comparing the three states HP, HS and LP and their cracking behaviour, the volume fraction of MC and borides, and their size increases with decreasing cooling rate. The increasing particle size is correlated with an increasing crack density, as shown in the simulation results (Table 5) and HE-XRD (Fig. 6). Additionally, HE-XRD results (Fig. 6) show the increase of γ‘-volume fraction. It can be argued, that due to the higher amounts of secondary phases, and formation of carbides and γ‘-films, the grain boundaries become prone to liquation cracking [66], e.g. by blocking the liquid channels for further melt feeding. As a second effect, the precipitates observed at lower cooling rates, are arranged in an inhomogeneous distribution of larger MC, boride and γ‘-particles at grain boundary triple points. It can be argued that the stress accumulation at these precipitation blocks is higher and cracks can be initiated more easily for HP in comparison to HS and LP conditions [67].

4.4. *Critical assessment of hot cracking susceptibility according to CSC and Kou-index*

In order to consider the impact of cooling rate on the hot cracking susceptibility, a few models have been suggested in the literature. The cracking susceptibility coefficient (CSC) after Clyne and Davies [68] and the Kou-index based on simulated solidification curves [69] are rather popular because they are easy to use. Both have been also applied to PBF-LB/M of nickel-based superalloys in the past (e.g. Refs. [70,71]). In the following, we compare the model predictions using the solidification curves from the phase-field simulations with the experimental findings.

In the literature, slightly different definitions can be found for CSC and Kou-index, mainly resulting from a different definition of the critical phase fraction intervals. We have used the following definitions:

$$CSC = \frac{t_v}{t_r} \tag{5}$$

with t_v vulnerable time for cracking, time between fraction liquid = 10 % and 1 % and t_r, time when stress relieve is possible, between 60 % und 10 % fraction liquid.

$$Average\ Kou = \frac{\partial T}{\partial\left(\sqrt{f_s}\right)} \tag{6}$$

with f_s average values between fraction solid = 92 % and 99 %.

Both coefficients are calculated based on the phase-field simulation results. The values are listed in Table 9. According to both criteria, LP and HS show a smaller cracking susceptibility in comparison to HP, consistent with the experimental findings. When comparing LP and HS, the calculation would predict a smaller cracking susceptibility for HS than for LP, contrary to the experimental observation. This deviation can be either explained by limitations in the models itself, or by the statistical nature of the phase formation. CSC was developed for iron-based alloys and Kou for aluminium alloys, in general for casting conditions with a much lower cooling rate compared to PBF-LB/M. This could mean that some of the underlying assumptions regarding the microstructure and liquid feeding are not fully applicable to the very fine dendritic morphologies obtained by PBF-LB/M. On the other hand, a statistically

Table 9
Calculated cracking susceptibility according to CSC and Kou.

	HP	HS	LP
CSC	0.78	0.47	0.73
Average Kou	130	75	95

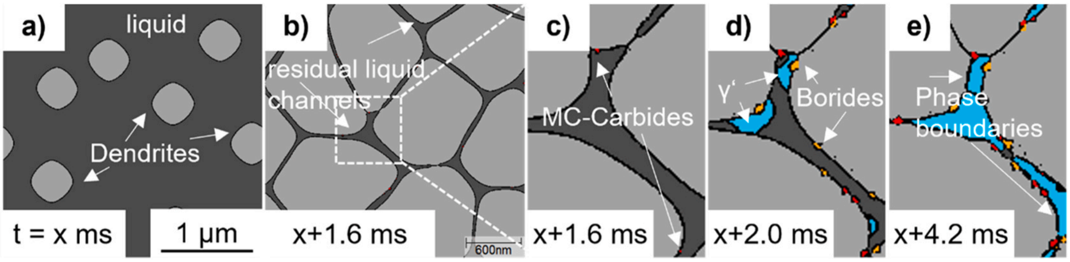

Fig. 12. Microstructure simulation results for the LP state: a) Dendritic growth (dark grey: melt, light grey fcc-Ni/γ); b) coalescence of dendrites with interdendritic liquid channels; c) MC-carbides (red); d) borides (orange) and γ’ (light blue) nucleating and growing at the fcc/melt interface; e) cutout from the fully solidified structure.

valid simulation analysis should take into account the stochastic nature of the nucleation, e.g. require a parameter study on the effect of the nucleation model parameters on the solidification path.

5. Conclusions

This comprehensive study investigates the relationship between PBF-LB/M process parameters, the resulting thermal conditions governing the solidification and the resulting solidification microstructures for the non-weldable nickel-based superalloy CM247LC. In greater detail, the alloying element distribution, the size and distribution of precipitates like γ', carbides and borides were analysed for three distinctly different PBF-LB/M process conditions, i.e. processing with high power, with low power and with a high laser scanning speed.

From a wide process parameter study, it is concluded that the crack density can be reduced by choosing process parameters resulting in a low linear energy input. A very low crack density of 0.23 mm/mm^2 could be achieved, which is the lowest crack density yet reported, without preheating, chemical modification or HIP. The reduction in the energy input leads to a significant increase in the cooling rate, which raises the question whether the microstructure and the phase formation, in particular near the end of solidification is significantly different for the different thermal conditions in a way that it can explain the achieved reduction of the crack density. The microstructure differences due to the different process parameters were investigated by combined process and microstructure simulations. Especially, the phase fractions and their formation over time have been analysed and quantified in detail for the various process parameters.

The following conclusions can be drawn.

1. PBF-LB/M processes with lower linear energies can lead to nearly crack free samples from the high γ' nickel-based alloy CM247LC.
2. Melt pool aspect ratio could be directly correlated with the crack density. Due to an increased mushy zone size with increasing cooling rate and, consequently, more susceptibility to hot cracking. These findings contrast with current literature findings, where the melt pool size was correlated to crack density.
3. Microsegregation and precipitates have been analysed using TEM-EDS and APT. The segregation pattern and the elemental composition of the precipitates are in good agreement with simulations applying a CALPHAD coupled phase-field model.
4. CALPHAD coupled phase-field simulations enables a quantitative analysis of the effect of cooling rate on the solidification path, e.g. the phase formation sequence, phase fractions and the size and location of precipitates in the microstructure.
5. An increase in cooling rate from 65,000 K/s to 570,000 K/s leads to a decrease of carbide fraction and carbide particle size as well as primary γ‘-size and fraction. The finer precipitates correlate with a decreasing crack susceptibility.
6. A possible microstructure related reason for the high crack density at lower cooling rates could lay in larger and inhomogeneously distributed precipitates as predicted by the simulations. Larger precipitates can impede the shrinkage induced melt feeding deep in the mushy zone, at grain boundary areas or between the dendrites. They could also lead to localised stress concentrations during thermal shrinkage. Both effects promote the crack formation.
7. A calculation of the crack susceptibility, either by CSC or based on the Kou-index, from the simulated solidification path for three different cooling rates confirms the higher crack density for smaller cooling rates $6.5 \cdot 10^4$ K/s (high power HP process) but does not reproduce the differences at higher cooling rates, i.e. between $3.5 \cdot 10^5$ K/s (high speed HS) and $5.7 \cdot 10^5$ K/s (low power LP).

As a general conclusion we would like to state that, according to this study, the experimentally observed process dependent hot cracking susceptibility, i.e. depending on the linear energy and the resulting cooling rate, for the PBF-LB/M processed nickel-based superalloy CM247LC cannot be explained solely by differences in the formation of the solidification microstructure, e.g. microsegregation and carbide or boride formation. This would imply that a better prediction of hot cracking susceptibility requires a more holistic approach, e.g. by integrating thermomechanical stresses at the melt pool and mush zone scales. Therefore, hot cracking criteria based solely on thermodynamic alloy properties appear to be limited.

CRediT authorship contribution statement

Philipp Stich: Writing – original draft, Visualization, Validation, Methodology, Investigation, Formal analysis, Data curation, Conceptualization. **Markus Apel:** Writing – review & editing, Methodology, Visualization, Formal analysis, Investigation. **Mustafa Megahed:** Investigation, Formal analysis. **Ludo Bautmans:** Conceptualization. **Pere Barriobero Vila:** Investigation, Formal analysis. **Marcus Hans:** Writing – review & editing, Investigation, Formal analysis. **Thomas Weirich E.:** Investigation, Formal analysis. **Klaus Büßenschütt:** Writing – original draft, Writing – review & editing. **Johannes Henrich Schleifenbaum:** Writing – review & editing, Funding acquisition. **Christian Haase:** Writing – review & editing, Supervision, Funding acquisition.

Declaration of competing interest

The authors declare that they have no known competing financial interests or personal relationships that could have appeared to influence the work reported in this paper.

Acknowledgments

This research is funded by the Digital Photonic Production DPP Research Campus (Funding number: 13N15423) as part of the "Research Campus Public-Private Partnership for Innovation" research funding initiative of the German Federal Ministry of Education and Research (BMBF). As part of the German government’s high-tech strategy, the BMBF is using this initiative to promote strategic and long-term cooperation between science and industry "under one roof". CH also acknowledges the support of the BMBF within the NanoMatFutur project “MatAM - Design of additively manufactured high performance alloys for automotive applications” (project ID 03XP0264) and of the Deutsche Forschungsgemeinschaft (DFG) within the project “H2MAT3D - Analysis of the interaction between hydrogen-based combustion systems, high-temperature materials and laser-based additive manufacturing” (project ID 523879740). MH is grateful for support by Deutsche Forschungsgemeinschaft (DFG) within the Collaborative Research Center SFB 1394, Structural and Chemical Atomic Complexity – From Defect Phase Diagrams to Materials Properties“ (project ID 409476157). The authors thank Mr. Sebastian Zischke (GFE) for performing the TEM measurements.

Appendix

Appendix 1. Chemical composition of Hf-rich precipitate displayed in Fig. 3 i) in wt.% obtained with SEM-EDS

Element	Ni [wt.%]	Cr [wt.%]	Co [wt.%]	Mo [wt.%]	W [wt.%]	Ta [wt.%]	Al [wt.%]	Ti [wt.%]	Hf [wt.%]
Point 1	21.26	3.26	3.32	0.15	0.96	3.72	4.99	0.44	61.91
Point 2	18.66	3.29	3.05	0	0.23	2.1	6.51	0.64	65.53

Appendix 2. Elemental distribution from 35 investigated carbides

Type	Ni	C	Cr	Co	Mo	W	Ti	Al	Ta	Hf	Zr
Carbide		+	+		(+)	+	+	(+)	+	+	(+)

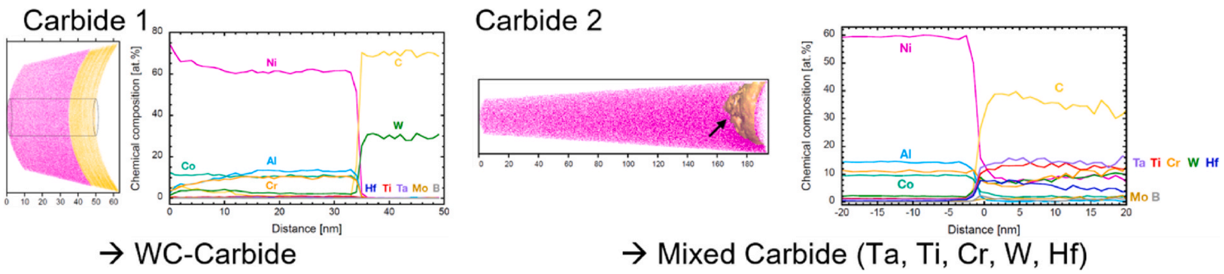

Appendix 3. APT measurements that got disrupted due to carbide breakoffs. Carbide 1 consist of C and W, while Carbide 2 consists of C with W, Ta, Ti, Cr, and Hf.

References

[1] Pant P, Salvemini F, Proper S, et al. A study of the influence of novel scan strategies on residual stress and microstructure of L-shaped LPBF IN718 samples. Mater Des 2022;214:110386. https://doi.org/10.1016/j.matdes.2022.110386.

[2] Guo W, Feng B, Yang Y, et al. Effect of laser scanning speed on the microstructure, phase transformation and mechanical property of NiTi alloys fabricated by LPBF. Mater Des 2022;215:110460. https://doi.org/10.1016/j.matdes.2022.110460.

[3] Köhnen P, Ewald S, Schleifenbaum JH, et al. Controlling microstructure and mechanical properties of additively manufactured high-strength steels by tailored solidification. Addit Manuf 2020;35:101389. https://doi.org/10.1016/j.addma.2020.101389.

[4] Binder M, Dirnhofer C, Kindermann P, et al. Procedure and validation of the implementation of automated sensor integration kinematics in an LPBF system. Proced CIRP 2020;93:1304–9. https://doi.org/10.1016/j.procir.2020.04.090.

[5] Sahasrabudhe H, Harrison R, Carpenter C, et al. Stainless steel to titanium bimetallic structure using LENS. Addit Manuf 2015;5:1–8. https://doi.org/10.1016/j.addma.2014.10.002.

[6] Shishkovsky I, Missemer F, Smurov I. Direct metal deposition of functional graded structures in Ti- Al system. Phys Procedia 2012;39:382–91. https://doi.org/10.1016/j.phpro.2012.10.052.

[7] Mageramova L, Vasilyev B, Kinzburskiy V. Novel designs of turbine blades for additive manufacturing. In: Volume 5C: heat transfer. American Society of Mechanical Engineers; 2016.

[8] Cieśla M, Binczyk F, Mańka M, et al. The influence of macrostructure of nickelbased superalloys IN713C and MAR 247 on the characteristics of high-temperature creep. Arch Foundry Eng 2014;14:11–6. https://doi.org/10.2478/afe-2014-0077.

[9] Thatte A, et al., editors. Multi-scale copled physics models and experiments for performance and life prediction of supercritical CO2 turbomachniery components; 2016.

[10] Stinville JC, Martin E, Karadge M, et al. Fatigue deformation in a polycrystalline nickel base superalloy at intermediate and high temperature: competing failure modes. Acta Mater 2018;152:16–33. https://doi.org/10.1016/j.actamat.2018.03.035.

[11] Gerstgrasser M, Cloots M, Stirnimann J, et al. Residual stress reduction of LPBF-processed CM247LC samples via multi laser beam strategies. Int J Adv Manuf Technol 2021;117:2093–103. https://doi.org/10.1007/s00170-021-07083-6.

[12] Griffiths S, Ghasemi Tabasi H, Ivas T, et al. Combining alloy and process modification for micro-crack mitigation in an additively manufactured Ni-base superalloy. Addit Manuf 2020;36:101443. https://doi.org/10.1016/j.addma.2020.101443.

[13] Adegoke O, Andersson J, Brodin H, et al. Influence of laser powder bed fusion process parameters on voids, cracks, and microhardness of nickel-based superalloy alloy 247LC. Materials (Basel) 2020;13. https://doi.org/10.3390/ma13173770.

[14] Catchpole-Smith S, Aboulkhair N, Parry L, et al. Fractal scan strategies for selective laser melting of 'unweldable' nickel superalloys. Addit Manuf 2017;15:113–22. https://doi.org/10.1016/j.addma.2017.02.002.

[15] Carter LN, Martin C, Withers PJ, et al. The influence of the laser scan strategy on grain structure and cracking behaviour in SLM powder-bed fabricated nickel superalloy. J Alloys Compd 2014;615:338–47. https://doi.org/10.1016/j.jallcom.2014.06.172.

[16] Carter LN, Attallah MM, Reed RC. Laser powder bed fabrication of nickel-base superalloys: influence of parameters; characterisation, quantification and mitigation of cracking. In: Huron ES, Reed RC, Hardy MC, et al., editors. Superalloys 2012. Hoboken, NJ, USA: John Wiley & Sons, Inc; 2012. p. 577–86.

[17] Engeli R. Selective laser melting & heat treatment of γ′ strengthened Ni-base superalloys for high temperature applications. ETH Zurich 2017.

[18] Berger R, Apel M, Laschet G. An analysis of the melt flow permeability for evolving hypoeutectic Al-Si mushy zone microstructures by phase field simulations. Materialia 2021;15:100966. https://doi.org/10.1016/j.mtla.2020.100966.

[19] Carter LN. Selective laser melting of nickel superalloys for high temperature applications. Dissertation: University of Birmingham; 2013.

[20] Fardan A, Fazi A, Peng RL, et al. Fine-tuning melt pools and microstructures: taming cracks in powder bed fusion—laser beam of a non-weldable Ni-base superalloy. Materialia 2024;34:102059. https://doi.org/10.1016/j.mtla.2024.102059.

[21] Kumar B, Sahu S, Srinivasan D, et al. Influence of heat input on solidification cracking in additively manufactured CM247LC Ni-based superalloy. Metall Mater Trans A 2023;54:2394–409. https://doi.org/10.1007/s11661-023-07027-7.

[22] Hilal H, Lancaster R, Stapleton D, et al. Investigating the influence of process parameters on the structural integrity of an additively manufactured nickel-based superalloy. Metals (Basel) 2019;9:1191. https://doi.org/10.3390/met9111191.

[23] Liu L, Di Wang, Deng G, et al. Crack inhibition to enhance strength-ductility of CM247LC alloy fabricated by laser powder bed fusion. Mater Sci Eng, A 2023;875:145114. https://doi.org/10.1016/j.msea.2023.145114.

[24] Gerstgrasser M, Cloots M, Stirnimann J, et al. Focus shift analysis, to manufacture dense and crack-free SLM-processed CM247LC samples. J Mater Process Technol 2021;289:116948. https://doi.org/10.1016/j.jmatprotec.2020.116948.

[25] Carter LN, Wang X, Read N, et al. Process optimisation of selective laser melting using energy density model for nickel based superalloys. Mater Sci Technol 2016;32:657–61. https://doi.org/10.1179/1743284715Y.0000000108.

[26] Chauvet E, Kontis P, Jägle EA, et al. Hot cracking mechanism affecting a non-weldable Ni-based superalloy produced by selective electron Beam Melting. Acta Mater 2018;142:82–94. https://doi.org/10.1016/j.actamat.2017.09.047.

[27] Cloots M, Kunze K, Uggowitzer PJ, et al. Microstructural characteristics of the nickel-based alloy IN738LC and the cobalt-based alloy Mar-M509 produced by selective laser melting. Mater Sci Eng, A 2016;658:68–76. https://doi.org/10.1016/j.msea.2016.01.058.

[28] Hariharan A, Lu L, Risse J, et al. Misorientation-dependent solute enrichment at interfaces and its contribution to defect formation mechanisms during laser

additive manufacturing of superalloys. Phys Rev Mater 2019;3. https://doi.org/10.1103/PhysRevMaterials.3.123602.

[29] Di Wang, Li S, Deng G, et al. A melt pool temperature model in laser powder bed fabricated CM247LC Ni superalloy to rationalize crack formation and microstructural inhomogeneities. Metall Mater Trans A 2021;52:5221–34. https://doi.org/10.1007/s11661-021-06457-5.

[30] Eagar TW, Tsai NS. Temperature fields produced by traveling distributed heat sources. Welding Res Suppl 1983;62:346–55.

[31] Duong E, Masseling L, Knaak C, et al. Scan path resolved thermal modelling of LPBF. Addit Manuf Lett 2022;3:100047. https://doi.org/10.1016/j.addlet.2022.100047.

[32] MICRESS version 7.1 and 7.2. www.micress.de.

[33] Böttger B, Apel M, Budnitzki M, et al. Calphad coupled phase-field model with mechano-chemical contributions and its application to rafting of γ’ in CMSX-4. Comput Mater Sci 2020;184:109909. https://doi.org/10.1016/j.commatsci.2020.109909.

[34] Carré A, Böttger B, Apel M. Implementation of an antitrapping current for a multicomponent multiphase-field ansatz. J Cryst Growth 2013;380:5–13. https://doi.org/10.1016/j.jcrysgro.2013.05.032.

[35] Böttger B, Seiz A, Sowa R, et al. Numerical prediction of primary dendrite arm spacing (PDAS), properties of the mushy zone, and freckle risk for various multicomponent Ni-base superalloys using the 3D-phase-field method. Comput Mater Sci 2024;236:112854. https://doi.org/10.1016/j.commatsci.2024.112854.

[36] Eiken J, Böttger B, Steinbach I. Multiphase-field approach for multicomponent alloys with extrapolation scheme for numerical application. Phys Rev E Stat Nonlin Soft Matter Phys 2006;73:66122. https://doi.org/10.1103/PhysRevE.73.066122.

[37] Boussinot G, Apel M, Zielinski J, et al. Strongly out-of-equilibrium columnar solidification during laser powder-bed fusion in additive manufacturing. Phys Rev Appl 2019;11. https://doi.org/10.1103/PhysRevApplied.11.014025.

[38] Boussinot G, Döring M, Schmidt M, et al. Strongly out-of-equilibrium growth morphologies in fast solidifying eutectics. Phys Rev Mater 2022;6. https://doi.org/10.1103/PhysRevMaterials.6.043405.

[39] Boussinot G, Döring M, Hemes S, et al. Laser powder bed fusion of eutectic Al–Ni alloys: experimental and phase-field studies. Mater Des 2021;198:109299. https://doi.org/10.1016/j.matdes.2020.109299.

[40] Böttger B, Apel M. Phase-field simulation of the formation of new grains by fragmentation during melting of an ABD900 superalloy. IOP Conf Ser Mater Sci Eng 2023;1281:12008. https://doi.org/10.1088/1757-899X/1281/1/012008.

[41] Pinomaa T, Provatas N. Quantitative phase field modeling of solute trapping and continuous growth kinetics in quasi-rapid solidification. Acta Mater 2019;168:167–77. https://doi.org/10.1016/j.actamat.2019.02.009.

[42] Uddagiri M, Shchyglo O, Steinbach I, et al. Phase-field study of the history-effect of remelted microstructures on nucleation during additive manufacturing of Ni-based superalloys. Metall Mater Trans A 2023;54:1825–42. https://doi.org/10.1007/s11661-023-07004-0.

[43] Kumara C, Balachandramurthi AR, Goel S, et al. Toward a better understanding of phase transformations in additive manufacturing of Alloy 718. Materialia 2020;13:100862. https://doi.org/10.1016/j.mtla.2020.100862.

[44] Tavakoli R, Tourret D. Phase-field study of polycrystalline growth and texture selection during melt pool solidification. IOP Conf Ser Mater Sci Eng 2023;1281:12011. https://doi.org/10.1088/1757-899X/1281/1/012011.

[45] Strunz P, Petrenec M, Davydov V, et al. Misfit in inconel-type superalloy. Adv Mater Sci Eng 2013;2013:1–7. https://doi.org/10.1155/2013/408347.

[46] den Broeder FJA, van Tendeloo G, Amelinckx S, et al. Microstructure of Cr100−xAlx alloys (10 at% ≲x ≲ 33 at%) studied by means of transmission electron microscopy and diffraction. II. Discovery of a new phase. Phys Stat Sol (a) 1981;67:233–48. https://doi.org/10.1002/pssa.2210670123.

[47] Wang X, Carter LN, Pang B, et al. Microstructure and yield strength of SLM-fabricated CM247LC Ni-Superalloy. Acta Mater 2017;128:87–95. https://doi.org/10.1016/j.actamat.2017.02.007.

[48] Rappaz M, Drezet J-M, Gremaud M. A new hot-tearing criterion. Metall Mater Trans A 1999;30:449–55. https://doi.org/10.1007/s11661-999-0334-z.

[49] Grange D, Bartout JD, Macquaire B, et al. Processing a non-weldable nickel-base superalloy by Selective Laser Melting: role of the shape and size of the melt pools on solidification cracking. Materialia 2020;12:100686. https://doi.org/10.1016/j.mtla.2020.100686.

[50] Stopyra W, Gruber K, Smolina I, et al. Laser powder bed fusion of AA7075 alloy: influence of process parameters on porosity and hot cracking. Addit Manuf 2020;35:101270. https://doi.org/10.1016/j.addma.2020.101270.

[51] Yang J, Li F, Wang Z, et al. Cracking behavior and control of Rene 104 superalloy produced by direct laser fabrication. J Mater Process Technol 2015;225:229–39. https://doi.org/10.1016/j.jmatprotec.2015.06.002.

[52] Barriobero-Vila P, Gussone J, Haubrich J, et al. Inducing stable α + β microstructures during selective laser melting of Ti-6Al-4V using intensified intrinsic heat treatments. Materials (Basel) 2017;10. https://doi.org/10.3390/ma10030268.

[53] Zhou YH, Li WP, Zhang L, et al. Selective laser melting of Ti–22Al–25Nb intermetallic: significant effects of hatch distance on microstructural features and mechanical properties. J Mater Process Technol 2020;276:116398. https://doi.org/10.1016/j.jmatprotec.2019.116398.

[54] Muñiz-Lerma JA, Tian Y, Wang X, et al. Microstructure evolution of Inconel 738 fabricated by pulsed laser powder bed fusion. Prog Addit Manuf 2019;4:97–107. https://doi.org/10.1007/s40964-018-0062-2.

[55] Li S, Wei Q, Shi Y, et al. Microstructure characteristics of inconel 625 superalloy manufactured by selective laser melting. J Mater Sci Technol 2015;31:946–52. https://doi.org/10.1016/j.jmst.2014.09.020.

[56] Weidong H, Xingguo G, Yaohe Z. Primary spacing selection of constrained dendritic growth. J Cryst Growth 1993;134:105–15. https://doi.org/10.1016/0022-0248(93)90015-O.

[57] Li Yuezu. Rapid solidification technology and new materials. 1993. p. 115 (in Chinese), Beijing.

[58] Hao Y, Li J, Li X, et al. Influences of cooling rates on solidification and segregation characteristics of Fe-Cr-Ni-Mo-N super austenitic stainless steel. J Mater Process Technol 2020;275:116326. https://doi.org/10.1016/j.jmatprotec.2019.116326.

[59] He C, Yu W, Li Y, et al. Relationship between cooling rate, microstructure evolution, and performance improvement of an Al–Cu alloy prepared using different methods. Mater Res Express 2020;7:116501. https://doi.org/10.1088/2053-1591/abc4f9.

[60] Collins LE, Barry JR. Reduced segregation in rapidly solidified CuNiSn alloys. Mater Sci Eng 1988;98:335–8. https://doi.org/10.1016/0025-5416(88)90181-4.

[61] Kundin J, Ramazani A, Prahl U, et al. Microstructure evolution of binary and multicomponent manganese steels during selective laser melting: phase-field modeling and experimental validation. Metall Mater Trans A 2019;50:2022–40. https://doi.org/10.1007/s11661-019-05143-x.

[62] Sarreal JA, Abbaschian GJ. The effect of solidification rate on microsegregation. Metall Trans A 1986;17:2063–73. https://doi.org/10.1007/BF02645003.

[63] Raghu R, Chandramohan P, Kumar DP, et al. Structural characterization and strength assessment of laser powder bed fusion manufactured CM247LC nickel based super alloy. J Mater Eng Perform 2023;32:11310–25. https://doi.org/10.1007/s11665-023-08550-9.

[64] Markanday JFS, Christofidou KA, Miller JR, et al. The microstructural evolution of CM247LC manufactured through laser powder bed fusion. Metall Mater Trans A 2023;54:1758–75. https://doi.org/10.1007/s11661-022-06939-0.

[65] Huang H-E, Koo C-H. Effect of zirconium on microstructure and mechanical properties of cast fine-grain CM 247 LC superalloy. Mater Trans 2004;45:554–61. https://doi.org/10.2320/matertrans.45.554.

[66] Thompson RG, Mayo DE, Radhakrishnan B. The relationship between carbon content, microstructure, and intergranular liquation cracking in cast nickel alloy 718. Metall Trans A 1991;22:557–67. https://doi.org/10.1007/BF02656823.

[67] Jiang R, Bull DJ, Evangelou A, et al. Strain accumulation and fatigue crack initiation at pores and carbides in a SX superalloy at room temperature. Int J Fatig 2018;114:22–33. https://doi.org/10.1016/j.ijfatigue.2018.05.003.

[68] Clyne TW, Davies GJ. Solidification and casting of metals. 1979. p. 275–8.

[69] Kou S. A criterion for cracking during solidification. Acta Mater 2015;88:366–74. https://doi.org/10.1016/j.actamat.2015.01.034.

[70] Wahlmann B, Leidel D, Markl M, et al. Numerical alloy development for additive manufacturing towards reduced cracking susceptibility. Crystals (Basel) 2021;11:902. https://doi.org/10.3390/cryst11080902.

[71] Tang YT, Panwisawas C, Ghoussoub JN, et al. Alloys-by-design: application to new superalloys for additive manufacturing. Acta Mater 2021;202:417–36. https://doi.org/10.1016/j.actamat.2020.09.023.